CHARGE TRANSFER EFFICIENCY AND OPTICAL PROPERTIES OF P3HT/PCBM SPIN COATED THIN FILMS

by

BRIAN ABRAHAM VAN HEERDEN

Submitted in fulfilment of
the requirements of the degree of

MASTER OF SCIENCE

in the

DEPARTMENT OF PHYSICS
UNIVERSITY OF THE WESTERN CAPE

SUPERVISOR : **PROF. C. J. ARENDSE**
Department of Physics, University of the Western Cape

CO-SUPERVISOR : **DR. G. F. MALGAS**
Materials Science and Manufacturing, Council for Scientific and Industrial Research

OCTOBER 2009

i

This thesis is dedicated to:

My mother, *Rosaline*

and late father,

Nicholas van Heerden

KEY WORDS

CHARGE TRANSFER EFFICIENCY AND OPTICAL PROPERTIES OF P3HT/PCBM SPIN COATED THIN FILMS

BRIAN ABRAHAM VAN HERRDEN

Photovoltaics

Charge transfer

Organic

Fullerene

Photoconductive

Efficiency

X-ray diffraction

Raman spectroscopy

Spin coating

Photoluminescence

ABSTRACT

CHARGE TRANSFER EFFICIENCY AND OPTICAL PROPERTIES OF P3HT/PCBM SPIN COATED THIN FILMS

BRIAN ABRAHAM VAN HEERDEN

M.Sc. Thesis, Department of Physics, University of the Western Cape

The efficiency of organic photovoltaics is influenced by the structure of the polymer, the morphology of the film, the interfaces between the layers, the choice of electron acceptor material and the ratio between the electron acceptor material and the polymer. In this project, we have used regioregular poly (3-hexylthiophene) (rr-P3HT) as the electron donor material and [6,6]-phenyl-C_{61}-butyric acid methyl ester (PCBM), a derivative of the C_{60} fullerene, as the acceptor material. Different weight-ratios of rr-P3HT to PCBM were prepared by stirring for several hours in a chloroform solution and subsequently spin coated onto crystalline silicon and transparent conductive oxide/glass substrates.

The effect of the PCBM concentration on the photo-induced optical emission and absorption properties of rr-P3HT was investigated by photoluminescence and ultraviolet-visible spectroscopy, respectively. Changes in the structural properties, as a function of the weight-ratio, were probed by high-resolution transmission electron microscopy, x-ray diffraction, Fourier transform infrared spectroscopy and Raman spectroscopy. Results show that the structural integrity and crystallinity of rr-P3HT is compromised with the addition of excessive amounts of PCBM, which has a negative impact on the optical absorption of rr-P3HT and the photo-induced charge transfer mechanism between the rr-P3HT and PCBM. This work illustrates that blending rr-P3HT with an equal weight of PCBM results in an optimum configuration for improved performance in organic photovoltaic devices.

OCTOBER 2009

DECLARATION

I declare that

"CHARGE TRANSFER EFFICIENCY AND OPTICAL PROPERTIES OF P3HT/PCBM SPIN COATED THIN FILMS"
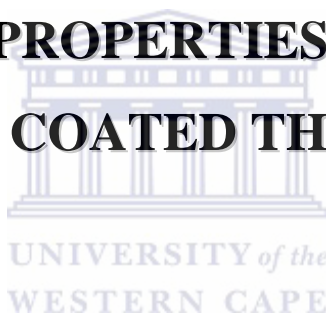
is my own work, that it has not been submitted for any degree or examination in any other university, and that all the sources I have used or quoted have been indicated and acknowledged by means of complete references.

BRIAN ABRAHAM VAN HEERDEN   **OCTOBER 2009**

SIGNED: …..………………………..

ACKNOWLEDGEMENTS

I would not have been able to complete this thesis without the help, guidance and support from the following people and organisations.

Prof. Christopher Arendse (Department of Physics, University of the Western Cape) for the exceptional supervision, guidance, friendship and the sustained support throughout the duration of this thesis

Dr. Gerald Malgas (National Centre for Nano-Structured Materials, Council for Scientific and Industrial Research) and Prof. Dirk Knoesen (Department of Physics, University of the Western Cape) who acted as co-supervisors, for their constant encouragement, guidance, friendship and many fruitful discussions

Mr. Theo Muller (Department of Physics, University of the Western Cape), fellow student and friend, for his constant encouragement, guidance, friendship and many fruitful discussions

Mr. David Motaung (National Centre for Nano-Structured Materials, Council for Scientific and Industrial Research), fellow student and friend, for his help with the preparation of the thin films and all the help with most of the analysis techniques

Prof. Basil Julies, Dr. Frik Koch and Mr. Adrian Josephs (Electron Microscopy Unit, University of the Western Cape) for their unselfish help and assistance during the electron microscopy studies.

The staff of the Physics Department of University of the Western Cape for their support and encouragement

To my family and friends, for the continuous love and support

Thank you!!

CONTENTS

CHAPTER 1

Introduction

1.1 PHOTOVOLTAICS: OVERVIEW

Fossil fuels possess very useful characteristics not shared by non-conventional energy sources (such as solar) that have made them popular during the last century. Unfortunately, fossil fuels are not renewable. The pollutants emitted by fossil energy systems, which include carbon dioxide, carbon monoxide, hydrocarbons, sulphur- and nitrous oxides, heavy metals and ashes, are also greater and more damaging than those that might be produced by renewable based energy systems. Fossil fuel alternatives, such as solar energy, are moving to the forefront in a variety of such fields. One such field is photovoltaic (PV) devices, which operate via the photovoltaic effect by employing the direct conversion of solar energy or sunlight into electrical power by means of a PV device or solar cell.

The first inorganic solar cell was developed at Bell Laboratories in 1954 [1.1]. It was based on crystalline silicon (c-Si), with an efficiency of 6%. Over the years the efficiency has reached 24% for these cells in the laboratory [1.2]. Today Si-based solar cells are by far the most dominating type of PV cell used and account for 99% of all PVs in the market [1.3].

With increasing efficiency and reduced production costs the world PV-market has increased. In the past 20 years, the demand for solar energy has grown consistently with annual growth rates of 20 – 25%. Fifty years of research and innovation has dramatically reduced the price of c-Si PVs to the level possible using existent technology. However, despite much effort of further reducing the price of c-Si based PVs, this technology is confined to niches. Thus, semiconductor PVs still account for less than 0.1% of the total world energy production.

Organic semiconductors are a less expensive alternative to inorganic semiconductors. Organic molecules can also be processed by techniques not available to crystalline inorganic semiconductors. In particular, the superior material properties of conjugated polymers, such as its low-cost, high strength to weight ratio, chemical resistance combined with a large number of cheap processing techniques, have made polymer-based materials present in almost every aspect of our modern society.

The first authentic investigations of organic photovoltaic (OPV) devices came in the 1950s, where a number of organic dyes, particularly chlorophyll and related compounds, were studied. In the 1980s the first polymers (including poly(sulphur nitride) and polyacetylene) were investigated in PV cells. However, simple PV devices based on dyes or polymers yield limited power conversion efficiencies (PCE), typically well below 0.1%. A major breakthrough came in 1986 when Tang discovered that bringing a donor and an acceptor together in one cell could dramatically increase the PCE to 1% [1.4]. Since the seminal work of Tang, organic solar cells have undergone a gradual evolution that has led to PCEs of about 5% [1.5-1.11]. Two main approaches have been explored in the effort to develop viable

devices: the donor-acceptor bilayer [1.11-1.13], commonly achieved by vacuum deposition of molecular components [1.14], and the so-called bulk heterojunction (BHJ), which is achieved by inter-dispersing the donor material and the acceptor material by blending to form a bi-continuous donor-acceptor composite active layer, thereby maximizing the all-important interfacial area between the donors and acceptors [1.15, 1.16]. Polymer-based photovoltaic systems that can be processed in solution and generally take the form of BHJ devices; most closely conform to the ultimate vision of organic solar cells as low-cost, lightweight and flexible devices. The real advantage of these BHJ devices, which can be processed in solution, as opposed to vacuum deposition, is the ability to process the composite active layer from solution in a single step, by using a variety of techniques that range from inkjet printing, spin coating and roller casting.
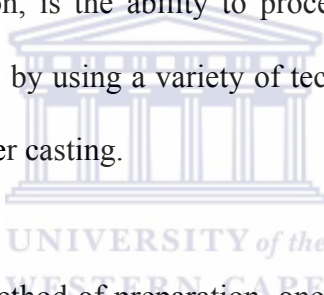
However, regardless of the method of preparation, one feature that extends across all classes of organic solar cells is the almost ubiquitous use of fullerenes and its derivatives as the electron-accepting component. The high electron affinity and superior ability to transport charge make fullerenes and its derivatives the best acceptor component currently available for these devices. The state-of-the-art in the field of organic photovoltaics is currently represented by BHJ solar cells based on poly(3-hexylthiophene) (P3HT) and the fullerene derivative [6,6]-phenyl-C_{61}-butyric acid methyl ester (PCBM), with reproducible efficiencies approaching 5% [1.6, 1.7]. To attain efficiencies approaching 10% in such organic solar cells, much effort is required to understand the fundamental electronic interactions between the polymeric donors and the fullerene acceptors as well as the complex interplay of device architecture, morphology, processing and the fundamental electronic processes.

1.2 CHARGE TRANSFER MECHANISM IN OPV DEVICES

When a semiconducting polymer absorbs incident solar radiation, an electron is excited from the highest occupied molecular orbital (HOMO) to the lowest unoccupied molecular orbital (LUMO), forming a electron-hole pair, known as an exciton [1.17]. The optical band gap is defined as the difference between the HOMO and the LUMO energy levels in a polymer, as illustrated in Figure 1.1. In a PV device this process must be followed by exciton dissociation. The electron must then reach one electrode while the hole must reach the other electrode. To achieve charge separation, an electrical field is required, which is provided by the asymmetrical ionisation energy/work functions of the electrodes. This asymmetry is the reason why electron-flow is more favoured from the low-work function electrode to the high work function electrode.
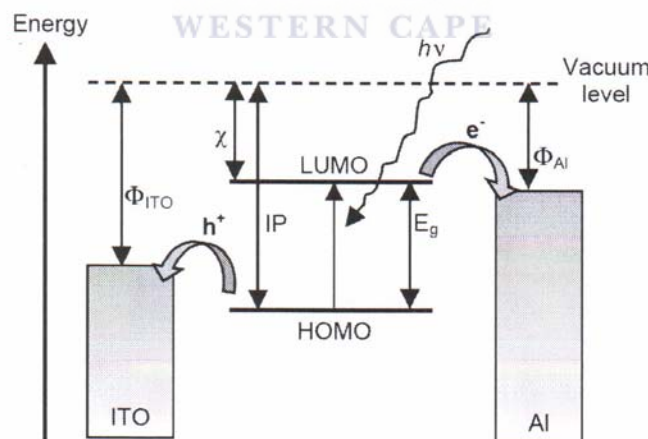

Figure 1.1   Upon irradiation an electron is promoted to the LUMO leaving a hole behind in the HOMO. Electrons are collected at the Al electrode and holes at the ITO electrode. Φ: workfunction, χ: electron affinity, IP: ionisation potential, E_g: optical band gap [1.17].

In the solid phase, the HOMOs and LUMOs of adjacent molecules may interact to produce a conduction band (CB) and a valance band (VB), respectively. The shape of the CB and VB changes when the organic material is put into contact with electrodes, depending on the conductance of the polymer and on whether the electrodes are connected or not.

In a crystalline inorganic semiconductor with a 3-dimensional (3D) crystal lattice the individual LUMOs and HOMOs form a CB and a VB throughout the material. This is fundamentally different from most organic dye semiconductors where the intermolecular forces are too weak to form 3D crystal lattices. Consequently, the molecular LUMOs and HOMOs do not interact strongly enough to form a CB and a VB. Thus, charge transport proceeds by hopping between localised states, rather than transport within a band. This implies that the charge carrier mobility in organic and polymeric semiconductors is generally low compared to inorganic semiconductors. Charge separation is also more difficult in organic semiconductors due to its low dielectric constant. In many inorganic semiconductors photon absorption produces a free electron and a hole (charge carriers), whereas the excited electron is bound to the hole in organic semiconductors. Conjugated polymers lie somewhere between the inorganic semiconductors and organic dyes. In general, excitons are considered as localised on specific chain segments. However, there are cases where excitons seem to be delocalised and are referred to as polarons [1.18].

In simple PV devices and diodes, based on organic semiconductors, the primary exciton dissociation site is at the electrode interface (other sites include defects in the crystal lattice, absorbed oxygen or impurities) [1.19]. This limits the effective light

harvesting thickness of the device, since excitons formed in the middle of the organic layer never reaches the electrode interface if the layer is too thick, resulting in recombination of the electron-hole pair. Typical exciton diffusion distances are on the order of 10 nm. As previously described, excitons do not dissociate readily in most organic semiconductors. The idea behind a heterojunction is to use two materials with different electron affinities and ionisation potentials. This will favour exciton dissociation: the material with the larger electron affinity will accept the electron and the material with the lower ionisation potential will accept the hole.

In 1979, Tang [1.4] filed a patent on his ability to increase PCE to 1% of a bi-layer PV device consisting of copper and a perylene derivative. Tang proposed that the observed synergistic effect of bringing two different semiconductors in contact was caused by the field at the heterojunction interface. This local field aids the dissociation of excitons diffusing to the interface. Such a situation is depicted in Figure 1.2 where the donor molecule is excited (upward arrow); the electron is promoted from the HOMO to the LUMO leaving a hole behind. The electron and hole can recombine (downward arrow), yielding luminescence, or they can dissociate. If the acceptor LUMO is sufficiently lower than the donor LUMO, the excited electron will relax into the acceptor LUMO and in this way be separated from the hole. Indeed, charge separation is much more efficient at the donor-acceptor interface than at the electrode interface.
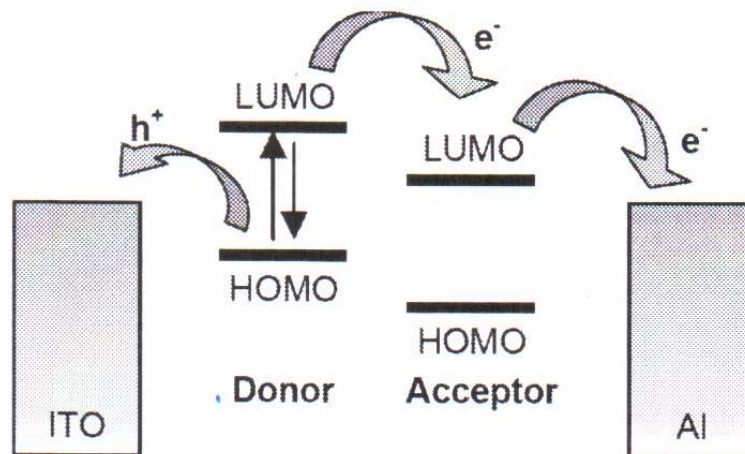
Figure 1.2   Exciton dissociation at the donor-acceptor interface. The electron migrates to the acceptor while the hole remains at the donor [1.17].

1.3 OPTIMISATION OF OPVs
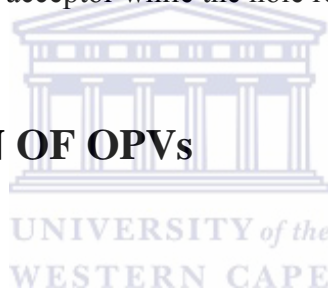
Efforts to optimise the performance of organic solar cells should find their basis in the fundamental mechanism of operation. Figure 1.3 illustrates the mechanism by which light energy is converted into electrical energy in the devices. The energy conversion process has four fundamental steps in the commonly accepted mechanism: (1) Absorption of light and generation of excitons, (2) diffusion of the excitons, 3) dissociation of the excitons with generation of charge, and (4) charge transport and charge collection [1.20].
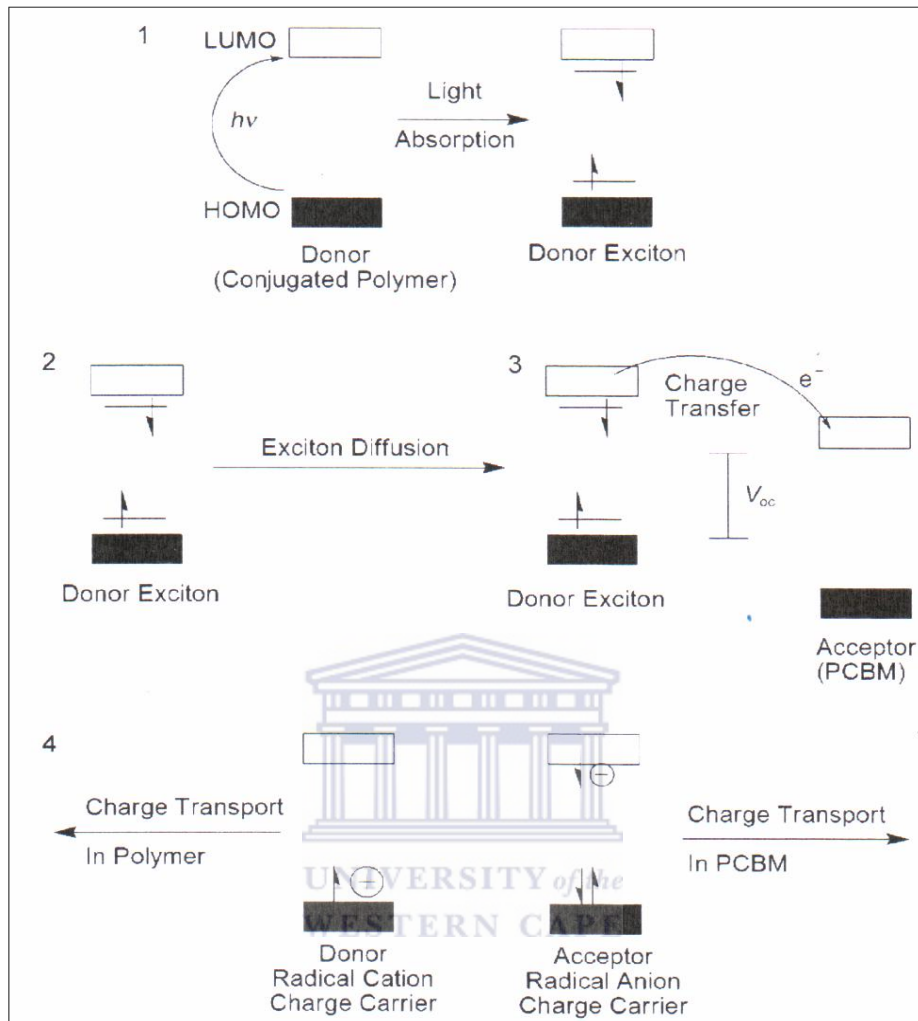
Figure 1.3   Mechanism for photo-energy conversion in excitonic solar cells [1.20].

Besides the fundamental mechanistic steps, the open circuit voltage (V_{oc}), which is defined as energy difference between the HOMO of the donor and the LUMO of the acceptor is also governed by the energetic relationship between the donor and the acceptor (Figure 1.3). It is therefore apparent that the choice of the components in the active layer as well as its morphology, which governs the physical interaction between the donor and acceptor, are the primary factors affecting the performance of the device [1.21, 1.22].

1.3.1 ELECTRONIC DONOR-ACCEPTOR INTERACTIONS

In principle, the optimisation of polymer-fullerene solar cells is based on fine-tuning the electronic properties and interactions of the donor and acceptor components so as to absorb the most light, generate the greatest number of free charges with minimal concomitant loss of energy, and transport the charges to the respective electrodes at a maximum rate and with a minimum of recombination. Such an approach focuses solely on the electronic characteristics of the individual components (absorption coefficient, charge carrier mobility) and ignores morphological issues that are also of critical importance in these devices.

The first constraint is that the donor must be capable of transferring charge to the fullerene upon excitation. A downhill energetic driving force is necessary for this process to be favourable and the driving force must exceed the exciton binding energy. This binding energy is the Coulombic attraction of the bound electron-hole pair in the donor, and typical values are estimated to be $0.4 - 0.5$ eV [1.23]. The energetic driving force effects the dissociation of the exciton with the formation of a geminate pair (step 3 in Figure 1.3). An additional energetic driving force is required to separate this geminate pair bound by Coulombic forces to generate free charges. This process is aided both thermally and by the intrinsic electric field in the device.

Empirically, the overall energetic driving force for a forward electron transfer from the donor to the acceptor is represented by the energy difference (offset) between the LUMOs of the donor and acceptor. It appears that a minimum energy difference of 0.3 eV is required to affect the exciton splitting and charge dissociation [1.24, 1.25].

Thus, the LUMO of an ideal polymer would reside at approximately 3.9 eV, since the LUMO energy for PCBM, the most commonly and successfully employed soluble fullerene derivative, is 4.2 eV.

The HOMO energy of the ideal donor polymer would then be determined by considering the band gap of the polymer, and hence the absorption of light, as well as the influence on the open circuit voltage (V_{oc}). The lower the energy of the HOMO, the greater the maximum theoretically attainable V_{oc}-value. However, the larger the band gap, the poorer the spectral overlap with the photon flux from the sun, which has a maximum at 1.8 eV (ca. 700 nm). Due to the large band gap in organic materials, only a small portion of the incident solar light is absorbed as illustrated in Figure 1.4 [1.26].
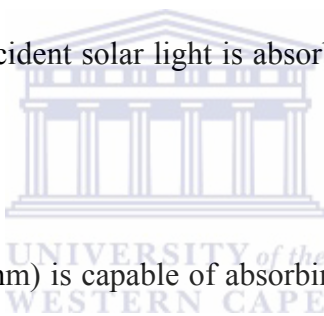
A band gap of 1.1 eV (1100 nm) is capable of absorbing 77% of the solar irradiation on earth [1.27]. However, the majority of semiconducting polymers have band gaps higher than 2 eV (620 nm), which limits the possible harvesting of solar photons to about 30%. On the other hand, because the absorption coefficients of organic materials are as high as 10^5 cm^{-1}, only 100 nm-thickness is enough to absorb most of the photons when a reflective back contact is used. A compromise is found by considering that a band gap of about 1.5 eV is an optimal value for a polymer absorber [1.28]. This gives a HOMO energy of about 5.4 eV, which corresponds to a maximum attainable V_{oc}-value of 1.2 V.
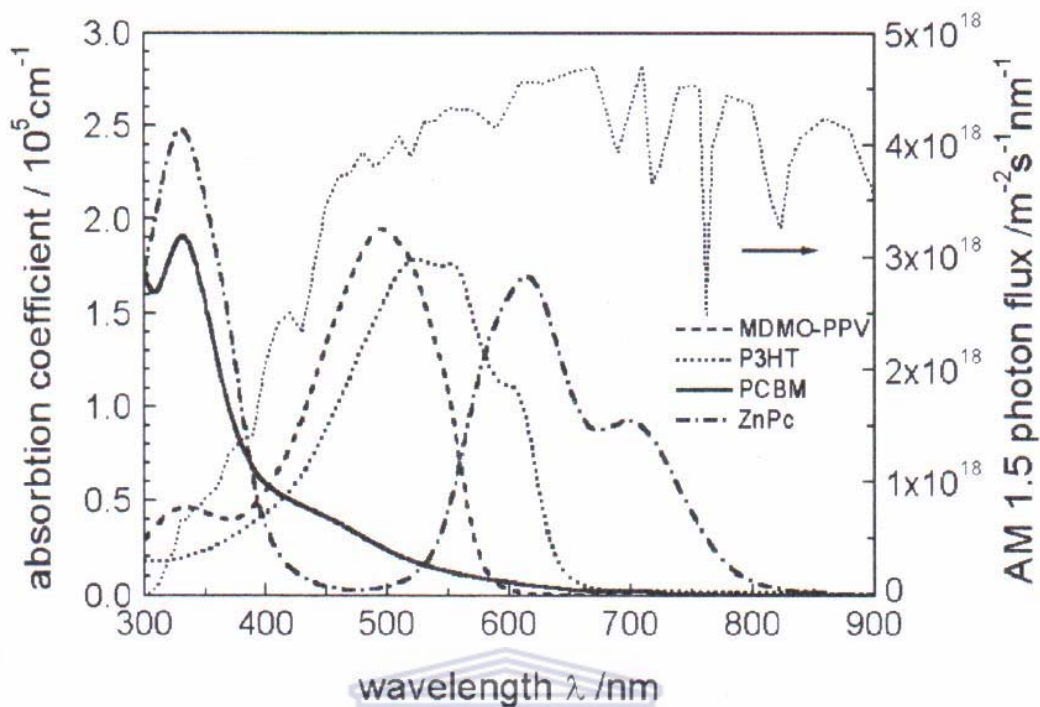
Figure 1.4   Absorption coefficients of films of commonly used materials are depicted in comparison with the standard AM1.5 terrestrial solar spectrum [1.26].

The optimal alignment of energy levels of the ideal polymer relative to the HOMO and LUMO energies of PCBM as well as that of MDMO-PPV (poly[2-methoxy-5-(3,7-dimethyloctyloxy)-1,4-phenylen]-alt-(vinylene)) and P3HT, two of the most commonly used donor polymers are illustrated in Figure 1.5.
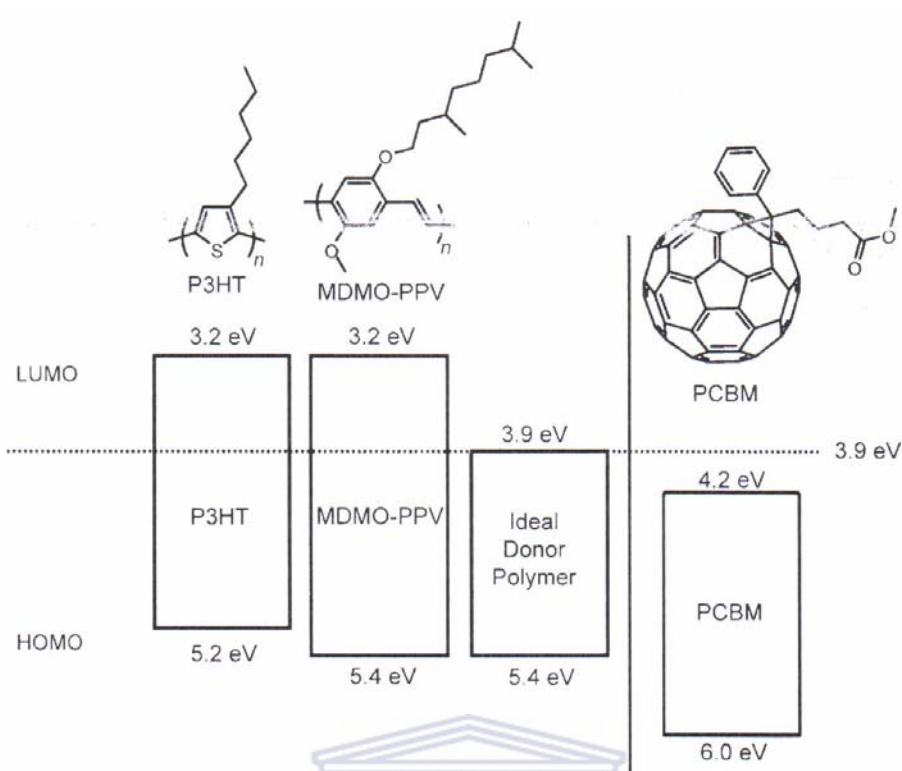
Figure 1.5 Band structure diagram illustrating the HOMO and LUMO energies of MDMO-PPV, P3HT, and an "ideal" donor relative to the band structure of PCBM. Energy values are reported as absolute values relative to a vacuum [1.20].

1.3.2 MORPHOLOGY

Even if the donor and acceptor have an ideal electronic relationship, the performance of bulk-heterojunction (BHJ) solar cells still depends on the physical interaction of the donor and acceptor components, which is manifested by the composite morphology. The ideal BHJ solar cell is defined as a bi-continuous composite of a donor and acceptor with a maximum interfacial area for exciton dissociation and a mean domain size commensurate with the exciton diffusion length (5 – 10 nm). The two components should phase-segregate on a suitable length scale to allow maximum ordering within each phase and thus effective charge transport in continuous pathways

to the electrodes so as to minimize the recombination of free charges. The composite should also be formed from solution and self-assemble into the most favourable morphology with the minimal application of external treatments, as well as having long-term stability.

The morphology of the active layer depends on the interplay between a number of intrinsic and extrinsic variables. The intrinsic properties are those that are inherent to the polymer and the fullerene, as well as the fundamental interaction parameters between the two components. These include the crystallinity of the two materials and their relative miscibility. The extrinsic factors include all the external influences associated with device fabrication, such as solvent choice, overall concentration of the blend components, deposition technique (spin coating, ink-jet printing, roller casting), solvent evaporation rate, as well as thermal and/or solvent annealing. It is clear that the number of factors affecting the morphology of the active layer is immense and specific to the polymer-fullerene pair used.

1.4 BASIC CONTRUCTION OF A BHJ OPV DEVICE

The general structure used for organic solar cells is similar to the organic light emitting diodes LEDs. The devices are fabricated in a sandwich geometry, as illustrated in Figure 1.6.
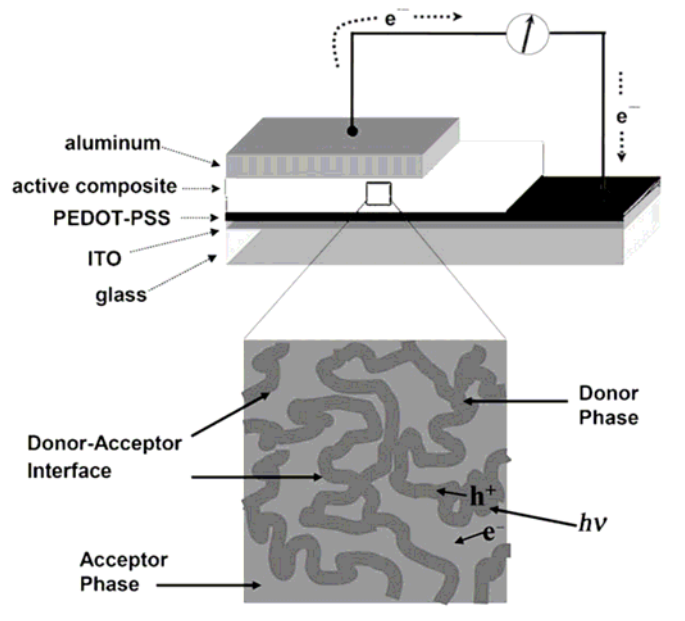
Figure 1.6   Device architecture for a thin film BHJ photovoltaic device [1.20].

A transparent, positive conducting electrode, such as indium-tin-oxide (ITO) coated on a glass or plastic is used as the substrate. On the transparent conducting substrate, poly(ethylene-dioxythiophene) doped with polystyrene-sulfonic acid (PEDOT:PSS) is coated from an aqueous solution. This PEDOT:PSS layer improves the surface quality of the ITO electrode (reducing the probability of electrical short-circuits) and facilitates the hole injection/extraction. Furthermore, the work function of this electrode can be changed by chemical/electrochemical redox reactions of the PEDOT layer. The work function of PEDOT:PSS amounts to ~ 5 eV *vs* vacuum, whereas the work function of ITO is rather undefined and reported to between 4.7 and 4.9 eV dependent on treatment [1.29, 1.30]. The ITO and PEDOT:PSS used in these devices, are highly transparent in the region between 350 and 900 nm.

The active layer, consisting of the conjugated polymer-fullerene mixture, is coated using solution or vacuum deposition techniques on top of PEDOT:PPS/ITO electrode. Finally, the top negative aluminium (Al) metal electrode with a lower work function (as compared to ITO) is evaporated on the active layer by physical vapour deposition techniques.

1.5 DEVICE EFFICIENCY

The current-voltage characteristics of a solar cell in the dark and under illumination are shown in Figure 1.7. In the dark, there is almost no current flowing, until the contacts start to inject at forward bias for voltages larger than the open circuit voltage. The device generates power under light illumination, with its maximum power point (P_m) in the fourth quadrant.
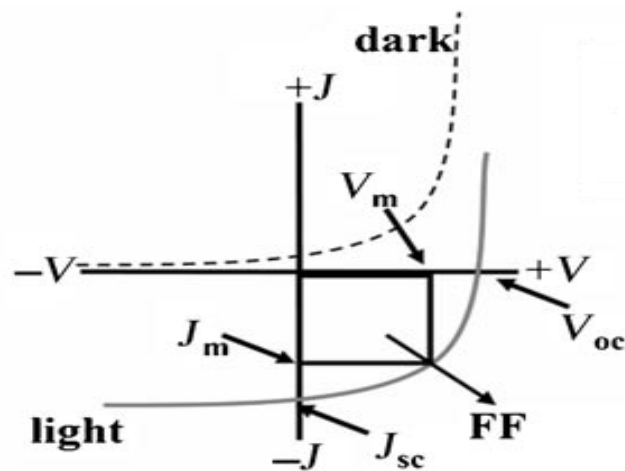
Figure 1.7 Current-voltage (J-V) curves of an organic solar cell illustrating the important parameters of such a device [1.20].

The photovoltaic power conversion efficiency (η) of a solar cell is determined by the following formula:

$$\eta = \frac{V_{oc} \times J_{sc} \times FF}{P_{in}} \qquad (1.1)$$

where:

$$FF = \frac{J_m \times V_m}{J_{sc} \times V_{oc}} \qquad (1.2)$$

where V_{oc} is the open circuit voltage, J_{sc} is the short circuit current density, FF is the fill factor, and P_{in} is the incident solar power density. This light intensity is standardized at 1000 W/m^2 with a spectral intensity distribution matching that of the sun on the earth's surface at an incident angle of 48.2°, which is called the AM1.5 spectrum [1.31]. J_m and V_m are the current density and voltage at the maximum power point, respectively.

1.5.1 OPEN CIRCUIT VOLTAGE

Generally, the open circuit voltage of a metal-insulator-metal (MIM) device is determined by the difference in work functions of the two metal contacts [1.32]. However, in a p-n junction, the maximum available voltage is determined by the difference of the quasi Fermi levels of the two charge carriers, i.e. n-doped semiconductor energy level and p-doped semiconductor energy level, respectively. In organic solar cells, the open circuit voltage is found to be linearly dependent on the HOMO level of the donor (p-type semiconductor quasi Fermi level) and the LUMO level of the acceptor (n-type semiconductor quasi Fermi level) [1.21, 1.33].

1.5.2 SHORT CIRCUIT CURRENT

In the ideal case for loss-free contacts, the short circuit current is proportional to the photo-induced charge carrier density and the charge carrier mobility within the organic semiconductors:

$$I_{sc} = ne\mu E \qquad (1.3)$$

where n is the density of charge carriers, e is the elementary charge, μ is the mobility, and E is the electric field. Assuming a 100% efficient process for the photo-induced charge generation in a bulk heterojunction mixture, n is the number of absorbed photons per unit volume.

1.6 MATERIAL PROPERTIES

1.6.1 POLYTHIOPHENES

Polythiophenes (PTs) result from the polymerisation of thiophenes, a sulphur heterocycle. The monomer structure of a PT unit is shown in the upper part of Figure 1.8 [1.34]. The most notable property of these materials, i.e. its electrical conductivity, results from the delocalisation of electrons along the polymer backbone − hence the term "synthetic metals". However, the electrical conductivity is not the only interesting property resulting from the electron delocalisation. The optical properties of these materials respond to environmental stimuli, with dramatic colour shifts in response to changes in solvent, temperature, applied potential and binding to other molecules. Both the colour changes and the electrical conductivity changes are

induced by the same mechanism, i.e. via the twisting of the polymer backbone or disrupting conjugation length.
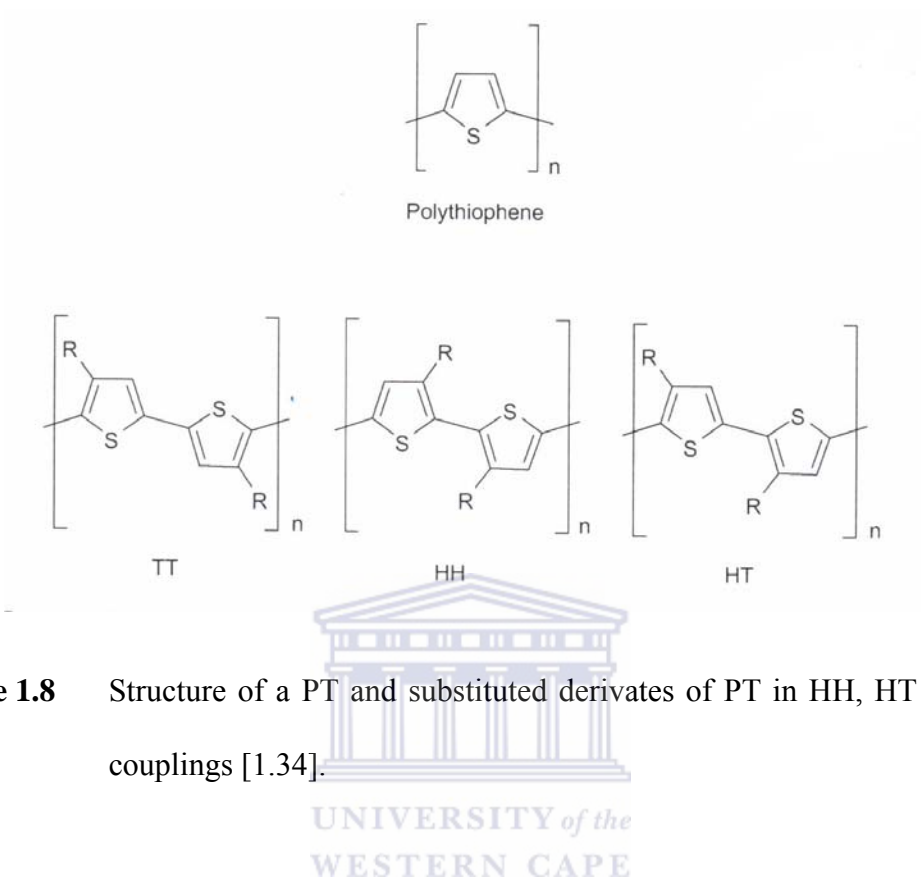
Figure 1.8   Structure of a PT and substituted derivates of PT in HH, HT and TT couplings [1.34].

1.6.1.1 Regioregularity

To improve the solubility of polythiophenes, many different R groups have been explored ranging from alkyl, alkoxy, acid, ester and phenyl groups. Since the thiophene ring is a 5-membered ring that is polymerised through the 2- and 5-position, substitution introduces directionality in the polymer and every time a monomer is incorporated in the growing polymer chain it can add with the head (2-position) or the tail (5-position) first. This gives the possibility for a regular material where all the molecules add in a head-to-tail (HT) fashion or it can be random with occasional head-to-tail (HT), head-to-head (HH) or tail-to-tail (TT) coupling. The lower part of Figure 1.8 shows the local structure resulting from the three possible couplings.

1.6.1.2 Conjugation Length

The extended π-systems of conjugated PTs produce some of the most interesting properties of these materials, i.e. their optical properties. Conjugation relies upon the overlap of the π-orbitals of the aromatic rings, which, in turn, requires the thiophene rings to be coplanar (see Figure 1.9, top).
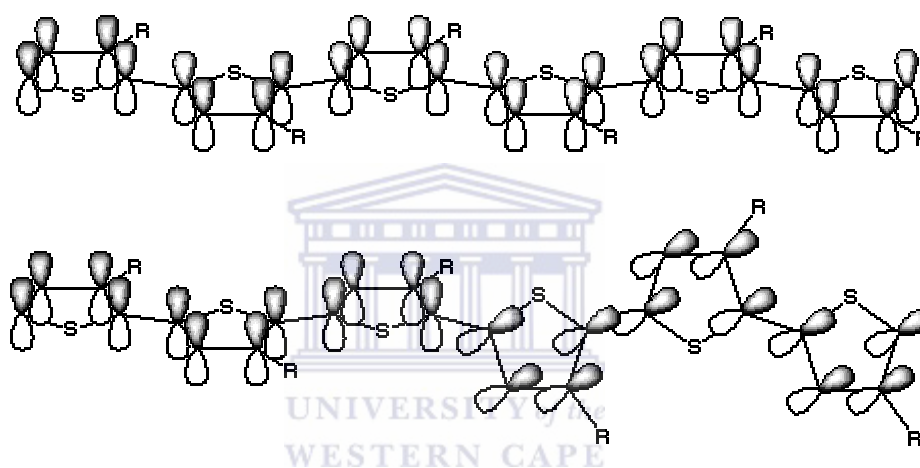
Figure 1.9   Conjugated π-orbitals of a coplanar and a twisted substituted PT.

The number of coplanar rings determines the conjugation length: the longer the conjugation length, the lower the separation between adjacent energy levels, and the longer the absorption wavelength. Deviation from co-planarity may be permanent, resulting from mislinkages during synthesis or especially bulky side chains; or temporary, resulting from changes in the environment or binding. This twist in the backbone reduces the conjugation length (see Figure 1.9, bottom), and the separation between energy levels is increased. This results in a shorter absorption wavelength.

1.6.1.3 Synthesis of Poly(3-hexylthiophene) (P3HT)

Polythiophenes were first synthesised in 1980 by two different chemical polymerisation methods, as outlined by Yamamoto et al [1.35] and Lin et al [1.36]. At the same time an electrochemical polymerisation of thiophene was reported [1.37]. However, these three types of polymerisation methods all resulted in insoluble polymer products. Consequently, several research groups strived to prepare soluble derivatives of polythiophene [1.38–1.40]. The poly-3-alkylthiophenes (PATs), first described in 1986, have four conformations: HT-HT, TT-HT, HT-HH and TT-HH. As described above the regularity of P3HT is of great importance due to higher conductivity of the polymer and higher efficiency of OPV devices. However, these synthetic methods did not give a regioregular polymer product. Highly regioregular P3HT (rr-P3HT) was not reported until the early 1990s by McCullough et al [1.41] and Reike et al [1.42] by two related methods, as illustrated in Figure 1.10. The regioregularity obtained from these synthetic procedures was 99% HT and 98.5% HT, respectively. The electrical conductivity of the rr-P3HT amounted to 1000 S/cm, as compared to 1 − 0.1 S/cm obtained for P3HT with a low regioregularity (58 − 70% HT) [1.43].
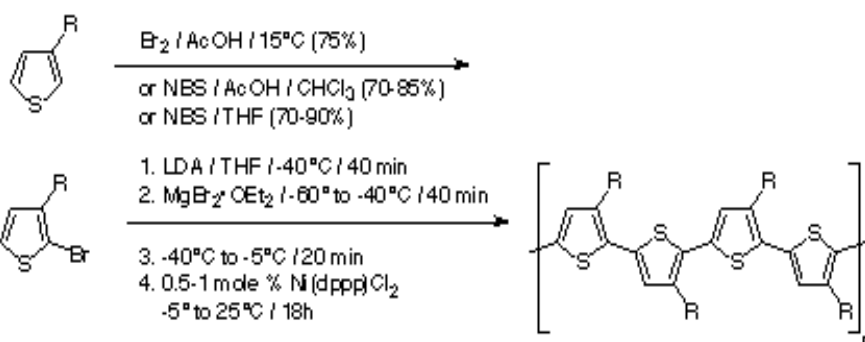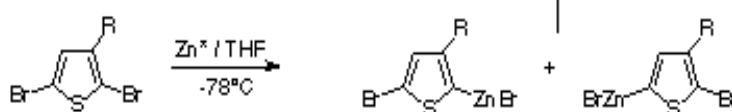
Figure 1.10   Different methods to produce rr-P3HT [1.41, 1.42].

1.6.1.4 Optical and Electrical Properties of rr-P3HT

Regioregular P3HT is one of the most studied conjugated polymers. Figure 1.11 depicts the structure of the P3HT polymer.
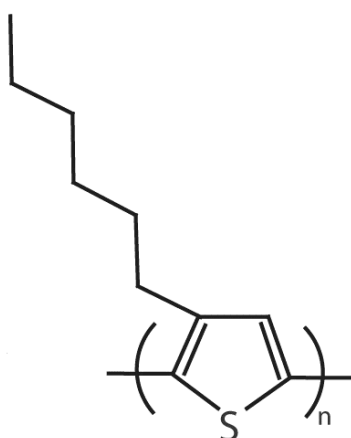

Figure 1.11   Chemical structure of the P3HT polymer.

The optical band gap of rr-P3HT is ~ 1.9 eV [1.44]. The characteristic absorption wavelength (λ_{max}) of P3HT and for poly-3-alkylthiophenes (PATs) varies with the percentage of head-to-tail coupling, i.e. the regularity of the side chains. Hence, the synthetic procedure leading to P3HT has a large influence on the properties of the final polymer product as discussed above. Furthermore, it has been shown that the absorption of P3HT depends on the molecular weight of the polymer [1.45], in that λ_{max} increases with an increase in molecular weight and the absorption spectrum becomes broader up to 600nm.

The regioregularity of P3HT is of great importance for the characteristics of the polymer, such as the electrical conductivity, the charge carrier mobility and charge transport. Several reports have investigated the regioregularity and its effect on packing of the polymer [1.45, 1.7]. It has been shown that rr-P3HT with a head-to-tail coupling stack in lamella (layerlike, crystallites) structure is separated by the side chains [1.47-1.52]. Hence, the length of the alkyl side chains affects the lamella structure only in the dimension of lamella thickness [1.51].

The solvent used for the spin coating of rr-P3HT thin films onto a variety of substrates has been shown to be of great importance [1.53, 1.54]. Films spin coated from chloroform was found to have their side chains directed towards the substrate [1.54]. It has also been shown that the drying time and drying mechanism affects the anisotropy of the polymer film [1.46, 1.47].

1.6.2 [6,6]-PHENYL-C$_{61}$-BUTYRIC ACID METHYL ESTER (PCBM)

Fullerene (C$_{60}$) molecules are currently considered to be the ideal acceptors for organic solar cells for several reasons. First, they have an energetically deep-lying LUMO [1.55], which endows the molecule with a very high electron affinity relative to the numerous potential organic donors. The triply degenerate LUMO of C$_{60}$ also allows the molecule to be reversibly reduced with up to six electrons, thus illustrating its ability to stabilize negative charges. Furthermore, C$_{60}$ has been shown to have a very high electron mobility of up to 1 cm^{2}V^{-1}s^{-1} in field-effect transistors (FETs) [1.56]. It is these fundamental properties that have made fullerenes one of the most important acceptor materials for BHJ solar cells. However, the solubility of the basic C$_{60}$ molecule is limited. Wudl [1.57] has synthesised a soluble derivative of C$_{60}$, i.e. [6,6]-phenyl-C$_{61}$-butyric acid methyl ester (PCBM), which has been widely used in polymer/fullerene solar cells due to its solubility and other properties inherent to all fullerenes [1.57]. Figure 1.12 shows the chemical structure of PCBM.
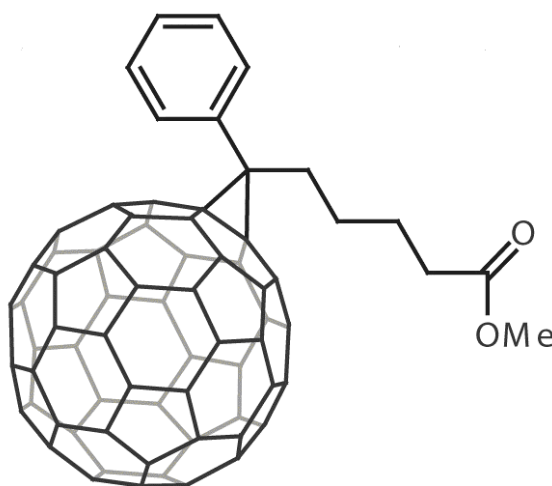

Figure 1.12   Chemical structure of PCBM.

1.7 AIMS AND OUTLINE

Over the last decade research activities into the use of photoconductive polymeric materials in the design of photovoltaic devices, i.e. organic photovoltaics (OPVs), have increased significantly. This is primarily due the low-cost, high processing speed and the ability to deposit it onto flexible substrates that the technology has to offer. One major drawback of OPVs is its low overall power conversion efficiency compared to the established inorganic solar cells, such as mono-crystalline silicon.

There are several factors that influence the efficiency of OPVs, i.e. the structure of the polymer, the morphology of the film, the interfaces between the layers, the choice of electron acceptor material and the ratio between the electron acceptor material and the polymer. Photoconductive polymers (electron-donors) that have been used to varying degrees of success are phthalocyanines, polythiophenes, and poly-phenylenevinylenes (PPV), while electron-acceptors that have been utilised are perylenes, nanorods, fullerenes, and nanotubes.

In this thesis, regioregular poly(3-hexylthiophene) (rr-P3HT) and [6,6]-phenyl-C_{61}-butyric acid methyl ester (PCBM) were used as the electron-donor and the electron-acceptor material, respectively. The aim of this investigation is to determine the optimal blend ratio of rr-P3HT:PCBM for an effective charge transfer mechanism and the subsequent improved efficiency in OPV devices. This will be achieved by blending rr-P3HT:PCBM in 1:1 and 1:4 weight ratios and investigating the effect of these blending ratios on the optical properties and relate this to the changes in the structural properties of rr-P3HT.

The outline of this thesis is as follows:

In *Chapter One* a general overview of photovoltaics was given. The chapter highlighted the current state of OPVs research around the world. Topics such as the charge transfer mechanism and optimisation in OPVs and the basic construction of an OPV device were discussed. In addition, the electron donor-acceptor materials that were used and their properties were also elucidated in this chapter.

Chapter Two will focus on the analysis techniques that will be used in this study to investigate the optical and structural properties of the blended rr-P3HT:PCBM thin films. Detailed theoretical background, upon which each technique is based, will be given.

Chapter Three we will report on the optical absorption and emission properties of spin-coated rr-P3HT:PCBM thin films. Specific emphasis will be on the changes induced in the optical properties of rr-P3HT by the loading of PCBM with different weight ratios.

Chapter Four will report on the effect of the different blend ratios on the structural properties of rr-P3HT when blended with PCBM. These results will be correlated to the changes in the optical properties discussed in the previous chapter.

Finally, general concluding remarks of Chapters Three and Four will follow in the *Summary*.

REFERENCES

[1.1]   D. M. Chapin, C. S. Fuller, G. L. Pearson, J. Appl. Phys. 25 (1954) 676

[1.2]   M. A. Green, K. Emery, D. L. King, S. Igari, W. Warta, Prog. Photovolt: Res. Appl. 11 (2003) 347

[1.3]   A. Goetzberger, C. Hebling, H. W.Chock, Mater. Sci. Eng. R 40 (2003) 1

[1.4]   C. W. Tang, Appl. Phys. Lett. 48 (1986) 183

[1.5]   B. A. Gregg, J. Phys. Chem. B 107 (2003) 4688

[1.6]   W. Ma, C. Yang, X. Gong, K. Lee, A. J. Heeger, Adv. Funct. Mater. 15 (2005) 1617

[1.7]   G. Li, V. Shrotriya, J. Huang, Y. Yao, T. Moriarty, K. Emery, Y. Yang, Nat. Mater. 4 (2005) 864

[1.8]   M. Reyes-Reyes, K. Kim, D. L. Carroll, Appl. Phys. Lett. 87 (2005) 083506

[1.9]   J. Xue, B. P. Rand, S. Uchida, S. R. Forrest, J. Appl. Phys. 98 (2005) 124903

[1.10]   J. Xue, B. P. Rand, S. Uchida, S. R. Forrest, Adv. Mater. 17 (2005) 66

[1.11]   J. Xue, S. Uchida, B. P. Rand, S. R. Forrest, Appl. Phys. Lett. 84 (2004) 3013

[1.12]   N. S. Sariciftci, D. Braun, C. Zhang, V. I. Srdanov, A. J. Heeger, G. Stucky, F. Wudl, Appl. Phys. Lett. 62 (1993) 585

[1.13]   M. Granstrom, K. Petritsch, A. C. Arias, A. Lux, M. R. Andersson, R. H. Friend, Nature 395 (1998) 257

[1.14]   P. Peumans, A. Yakimov, S. R. Forrest, J. Appl. Phys. 93 (2003) 3693

[1.15]   J. J. M. Halls, C. A. Walsh, N. C. Greenham, E. A. Marseglia, R. H. Friend, S. C. Moratti, A. B. Holmes, Nature 376 (1995) 498

[1.16]   G. Yu, A. J. Heeger, J. Appl. Phys. 78 (1995) 4510

[1.17]   H. Spanggaard, F. C. Krebs, Sol. Energy Mater. & Sol. Cells 83 (2004) 125

[1.18]   U. Rauscher, H. Bassler, D. D. C. Bradley, Phys. Rev. B 42 (1990) 9830

[1.19]   L. J. Rothberg, M. Yan, F. Papadimitrakopolous, M. E. Galvin, E. W. Kwock, T. M. Miller, Synth. Met. 80 (1996) 41

[1.20]   B. C. Thompson, M. J. Frechet, Angew. Chem. Int. Ed. 47 (2008) 58

[1.21]   C. J. Brabec, A. Cravino, D. Meissner, N. S. Sariciftci, T. Fromherz, M. T. Rispens, L. Sanchez, J. C. Hummelen, Adv. Funct. Mater. 11 (2001) 374

[1.22]   A. Gadisa, M. Svensson, M. R. Andersson, Appl. Phys. Lett. 84 (2004) 1609

[1.23]   V. I. Arkhipov, H. Bassler, Phys. Status Solidi A 201 (2004) 1152

[1.24]   C. J. Brabec, C. Winder, N. S. Sariciftci, J. C. Hummelen, A. Dhanabalan, P. A. van Hal, R. A. J. Janssen, Adv. Funct. Mater. 12 (2002) 709

[1.25]   C. Winder, G. Matt, J. C. Hummelen, R. A. J. Janssen, N. S. Sariciftci, C. J. Brabec, Thin Solid Films 403 (2002) 373

[1.26]   S. Gunes, H. Neugebauer, N. S. Saricifci, Chem. Rev. 107 (2003) 1324

[1.27]   J. M. Nunzi, Physique 3 (2002) 523

[1.28]   C. Soci, I. W. Hwang, D. Moses, Z. Zhu, D. Waller, R. Guandiana, C. J. Brabec , A. J. Heeger, Adv. Func Mater. 17 (2007) 632

[1.29]   G. Greczynski, Th. Kugler, M. Keil, W. Osikowicz, M. Fahlman, W. R Salanck, J. Electron Spectrosc. Relat. Phenom. 121 (2001) 1

[1.30]   J. S. Kim, M. Granstrom, R. H. Friend, N. Johansson, W. R. Salaneck, R. Daik, W. J. Feast, F. Cacialli, J. Appl. Phys. 84 (1998) 6859

[1.31]   J. Rostalski, D. Meissner, Sol. Energy Mater. & Sol. Cells 61 (2000) 87

[1.32]   I. J. Parker, Appl. Phys. 75 (1994) 1656

[1.33]   M. Scharber, D. Muhlbacher, M. Koppe, P. Denk, C. Waldauf, A. J. Heeger, C. Brabec, Adv. Mater. 18 (2006) 789

[1.34]   E. Bungaard, F. C. Krebs, Sol. Energy Mater. & Sol. Cells 91 (2007) 954

[1.35]   T. Yamamoto, K. Sanechika, A. Yamamoto, J. Pol. Sci. Pol. Lett. Ed. 18 (1980) 9

[1.36]   J. W. P. Lin, L. P. Dudek, J. Pol. Sci. Pol. Lett. Ed. 18 (1980) 2869

[1.37]   J. Roncali, Chem. Rev. 97 (1997) 173

[1.38]   M. Sato, S. Tanaka, K. Kaeriyama, J. Chem. Soc. Chem. Commun. 11 (1986) 873

[1.39]   K.-Y. Jen, G. G. Miller, J. Chem. Soc. Chem. Commun. 17 (1986) 1346

[1.40]   R. L. Elsenbaumer, K. Y. Jen, R. Oboodi, Synth. Met. 15 (1986) 169

[1.41]   R. D. McCullough, R. D. Lowe, D. L. Anderson, J. Org. Chem. 58 (1993) 904

[1.42]   T.-A. Chen, R. D. Reike, J. Am. Chem. Soc. 114 (1992) 10087

[1.43]   R. D. McCullough, Adv. Mater. 10 (1998) 93

[1.44]   L. J. A. Koster, V. D. Mihailetchi, P. W. M. Blom, Appl. Phys. Lett. 88 (2006) 093511

[1.45]   P. Schilinsky, U. Asawapirom, U. Scherf, M. Biele, C. J. Brabec, Chem. Mater. 17 (2005) 2175

[1.46]   D. W. Breiby, E. J. Samuelsen, O. Konovalov, Synth. Met. 139 (2003) 361

[1.47]   D. W. Breiby, E.J. Samuelsen, J. Pol. Sci. B: Pol. Phys. 41 (2003) 2375

[1.48]   K. E. Aasmundtveit, E. J. Samuelsen, W. Mammo, M. Svensson, M. R. Andersson, L. A. A. Pettersson, O. Inganas, Macromolecules 33 (2000) 5481

[1.49]   D. Fichou, J. Mater. Chem. 10 (2000) 571

[1.50]   H. J. Fell, E. J. Samuelsen, M. R. Andersson, J. Als-Nielsen, G. Grubel, J. Mardalen, Synth. Met. 73 (1995) 279

[1.51]   J. Mardalen, E. J. Samuelsen, Synth. Met. 48 (1992) 363

[1.52] T. J. Prosa, M. J. Winokur, J. Moulton, P. Smith, A. J. Heeger, Macromolecules 25 (1992) 4364

[1.53] K. E. Aasmundtveit, E. J. Samuelsen, M. Guldstein, C. Steinsland, O. Flornes, C. Fagermo, T. M. Seeberg, L. A. A. Pettersson, O. Inganas, R. Feidenhans'l, S. Ferrer, Macromolecules 33 (2000) 3120

[1.54] H. J. Fell, E. J. Samuelsen, J. Mardalen, M. R. Andersson, Synth. Met. 69 (1995) 283

[1.55] P. M. Allemand, A. Koch, F. Wudl, J. Am. Chem. Soc. 113 (1991) 1050

[1.56] T. B. Singh, N. Marjanovic, G. J. Matt, S. Gunes, N. S. Sariciftci, A. Montaigne Ramil, A. Andreev, H. Sitter, R. Schwodiauer, S. Bauer, Org. Electron. 6 (2005) 105

[1.57] F. Wudl, Acc. Chem. Res.25 (1992) 157161
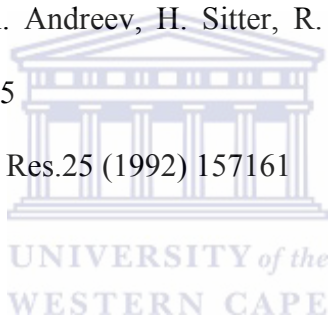
CHAPTER 2

Analytical Techniques

2.1 INTRODUCTION

The study of rr-P3HT blended with PCBM requires accurate and well-understood techniques. Table 2.1 presents the different characterisation techniques utilized in this study and the corresponding information each technique can provide about the optical and structural changes that occur when rr-P3HT is blended with different weight ratios of PCBM.
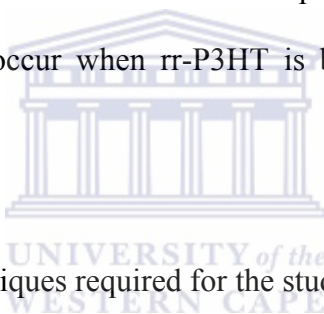
Table 2.1   Analytic techniques required for the study of rr-P3HT:PCBM blends.

Technique	Information
Ultraviolet-visible spectroscopy (UV-VIS)	Electronic structure, optical properties
Photoluminescence (PL)	Electronic structure, degree of quenching
Fourier transform infrared spectroscopy (FTIR)	Chemical structure
Raman spectroscopy	Chemical structure
X-ray diffraction (XRD)	Crystallinity, grain size and orientation
High-resolution transmission electron microscopy (HR-TEM)	Crystallinity, grain size and orientation

2.2 ULTRAVIOLET-VISIBLE SPECTROSCOPY

2.2.1 INTRODUCTION

Ultraviolet-visible (UV-VIS) involves the spectroscopy of photons in the UV-VIS region. This means it uses light in the visible and adjacent (near ultraviolet (NUV) and near infrared (NIR)) ranges. The absorption in the visible ranges directly affects the color of the chemicals involved. In this region of the electromagnetic spectrum, molecules undergo electronic transitions and UV-VIS absorption therefore measures transitions from the ground state to the excited state. Crucial to the power conversion efficiency of any photovoltaic device is the optical properties of the light absorbing material. In particular, the optical band gap is the most widely studied optical property for solar cell applications, since it is related to the electronic structure of the material and, more importantly, since the efficiency is directly related to it. In this study UV-VIS spectroscopy will be used to determine the optical band gap of rr-P3HT, estimated from the absorption band edge, and to report on the changes that are induced in the optical properties of rr-P3HT by the loading of PCBM with different weight ratios.

2.2.2 THEORY

Organic compounds, such as polymers, with a high degree of conjugation absorb radiation in the UV-VIS regions of the electromagnetic spectrum. When light impinges on a film, molecules within the film can undergo electronic transitions from the ground state to the excited state. The ratio of the radiation intensity transmitted by

the film of thickness x (I_x) to that transmitted by a known reference (I_o) is known as the transmittance (T) of the film and is given by:

$$T = \frac{I_x}{I_o} \qquad (2.1)$$

In practice we often measure percent transmittance (%T), because many instruments are calibrated with its very convenient scale of 0 to 100. A more useful quantity is the amount of radiation absorbed, referred to as the absorbance (A), given by:

$$A = \ln\left(\frac{I_0}{I_x}\right) = \ln\left(\frac{1}{T}\right) \qquad (2.2)$$
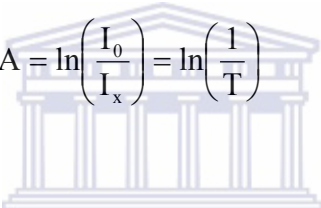
There is also a variety of energy absorptions possible depending upon the nature of the bonds within a molecule. For instance, electrons in organic molecules may be in strong σ bonds, in weaker π bonds or non- bonding, n. When energy is absorbed all of these type of electrons can be elevated to excited anti-bonding states that can be presented diagrammatically as in Figure 2.1, the anti-bonding states being represented with an asterisk as σ* and π*.

Most σ→σ* absorptions for individual bonds occur below 200 nm in the vacuum/ultraviolet region and compounds containing just the σ bonds are transparent in the near ultraviolet/visible regions. The π→ π* and n→ π* absorptions occur in the near ultraviolet/visible region, and result from the presence in molecules of unsaturated groups, known as chromophores.
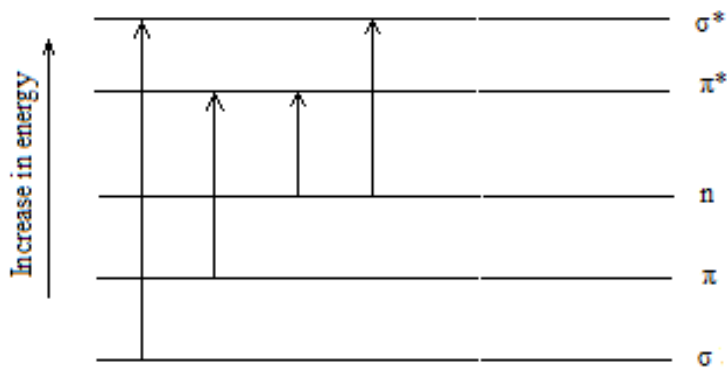
Figure 2.1   Bonding and anti-bonding energy transitions.

2.2.3 EXPERIMENTAL SET-UP

The basic parts of a typical spectrophotometer are a light source, a sample holder, a diffraction grating or monochromator to separate the different wavelengths of light, and a detector. The radiation source is often a Tungsten filament (300-2500 nm), a deuterium arc lamp that is continuous over the ultraviolet region (190-400 nm), or more recently light emitting diodes (LED) and Xenon arc lamps for the visible wavelengths. The detector is typically a photodiode or a charge-coupled (CCD) device. Photodiodes are used with monochromators, which filter the light so that only light of a single wavelength reaches the detector. Diffraction gratings are used with the CCD, which collects light of different wavelengths on different pixels. Figure 2.2 shows the layout of a typical spectrophotometer.

A spectrophotometer can be either single beam or double beam. In a single beam instrument (such as the one depicted in Figure 2.2), all of the light passes through the sample cell. I_o must be measured by removing the sample. In a double-beam instrument, the light is split into two beams before it reaches the sample. One beam is used as the reference while the other beam passes through the sample. Some double-

beam instruments have two detectors (photodiodes), and the sample and reference beam are measured at the same time. In other instruments, the two beams pass through a beam chopper, which blocks one beam at a time. The detector alternates between measuring the sample beam and the reference beam.
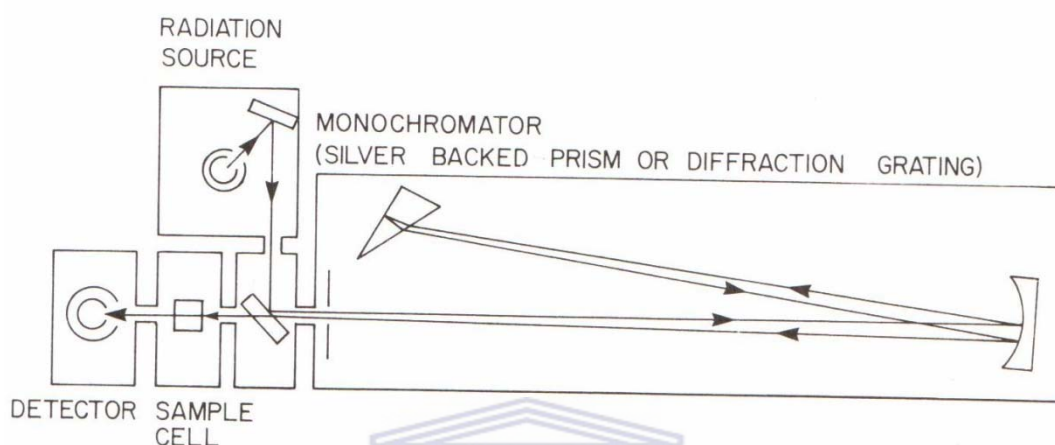
Figure 2.2   Layout of a single beam UV-VIS spectrophotometer [2.1].
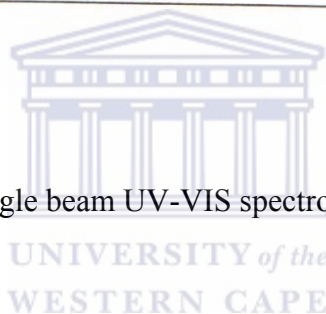
In this study, the optical absorption spectra of spin-coated rr-P3HT:PCBM thin films were measured from 200 – 900 nm, with a spectral resolution of 1 nm, using a Perkin-Elmer LAMDA 20 UV-VIS spectrophotometer (National Centre for Nano-Structured Materials, Council for Scientific and Industrial Research).

2.3 PHOTOLUMINESCENCE

2.3.1 INTRODUCTION

Photoluminescence (PL) is a process by which a substance absorbs photons and re-radiates it through various mechanisms. Therefore, this technique is widely used to

investigate the energy levels of materials, thereby providing fundamental information on the electronic properties and impurity levels of these materials. In addition to the information on the properties of the energy levels that can be obtained within rr-P3HT, the PL technique can also be used to study the interaction between rr-P3HT and PCBM when photo-excited. The reduction in the PL intensity, that is, the degree of quenching when rr-P3HT is loaded with PCBM is therefore a direct measure of the interaction between rr-PHT and PCBM when photo-excited.

2.3.2 THEORY

When recording PL spectra, the sample studied is excited with an optical source; usually a laser, with energy (hν) higher than the optical band gap (E_g) of the material under investigation. This results in the generation of electron-hole pairs (exciton) that recombine by one of several mechanisms, as shown in Figure 2.3. The energy of the photons emitted after recombination depends on the nature of the recombination processes involved. Figure 2.3 schematically describes common radiative transitions observed by photoluminescence [2.2].
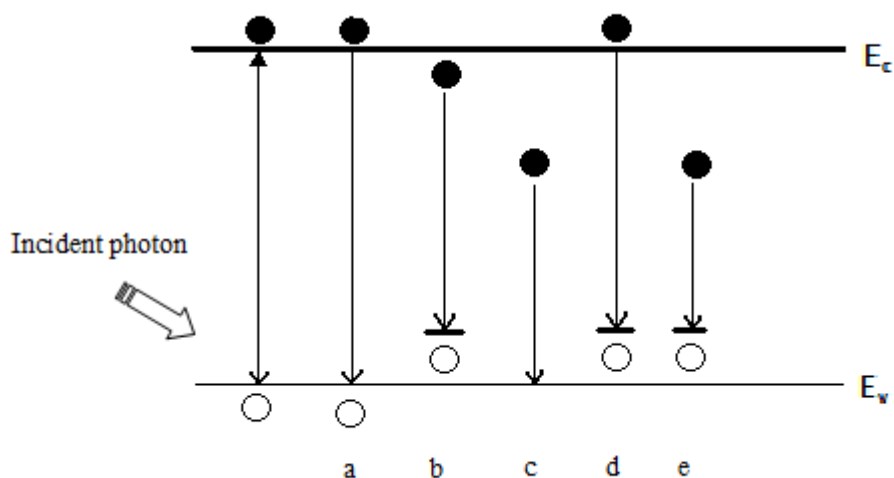

Figure 2.3   Radiative transitions observed by photoluminescence [2.2].

Band-to-band recombination, depicted in Figure 2.3 (a), is the most frequently occurring process at room temperature; on the other hand, it rarely takes place at low temperatures in materials with small effective masses due to large electron orbital radii and thermal quenching effects. Excitonic recombination, (b), represents a bound electron-hole pair in a hydrogen like state. The free exciton (FX) has energy slightly less than the band gap energy required to generate a separated electron-hole pair. In fact, a photon emitted by free exciton (FX) recombination has energy:

$$E = E_g - E_x \qquad (2.3)$$

where E_x is the exciton binding energy. Knowledge of the exciton binding energy enables one to accurately determine the band gap from the energy of the free exciton recombination. In doing so, however, distinguishing free excitonic emission from other excitonic or impurity-related lines is crucial. Furthermore, a free hole can combine with a neutral donor to form a positively charged excitonic ion, or donor-bound exciton (D°X), as illustrated in Figure 2.3 (c). Similarly, a free electron can combine with a hole on a neutral acceptor to form an acceptor-bound exciton, A°X (d). Finally, an electron on a neutral donor can recombine with a hole on a neutral acceptor; this is called donor-acceptor pair recombination (DAP), and is illustrated in Figure 2.3 (e). The Coulombic interaction between donors and acceptors results in the modification of the DAP emission line energy E, given by:

$$E = E_g - \left(E_A - E_D\right) + \frac{e^2}{\varepsilon \varepsilon_o r} \qquad (2.4)$$

where E_A and E_D is the donor and acceptor energy levels, respectively, r is the distance between donor and acceptor, ε the dielectric constant of the material, e is the electron change and ε_o is the permittivity of free space.

2.3.3 EXPERIMENTAL SET-UP

The PL spectra presented in this work were recorded on a scanning PL system schematically depicted in Figure 2.4 (Department of Physics, Nelson Mandela Metropolitan University). The samples investigated are fastened to the sample holder with vacuum grease, and are excited by the 325 nm line of a HeCd laser. The laser beam passes through a filter, and is then subjected to a chopper. The beam is consequently focused perpendicularly onto the sample surface after being reflected off a variable position mirror. The mirror is linked to an x-y motion controller, making it possible to position the laser anywhere on the sample surface. The emitted luminescence backtracks the signal up to the position mirror where it is deflected. It then passes through a high pass filter that removes the reflected laser beam. The photoluminescence is dispersed by a 0.5 m SPEX 1870 spectrometer, and detected by a water-cooled photo-multiplier tube (PMT). The output from the detector is finally amplified by a lock-in amplifier interfaced to a computer where the PL spectrum is viewed and analysed. The HeCd laser yielded a maximum power of 20 mW, which could be reduced by inserting optical density filters between the chopper and the position mirror.
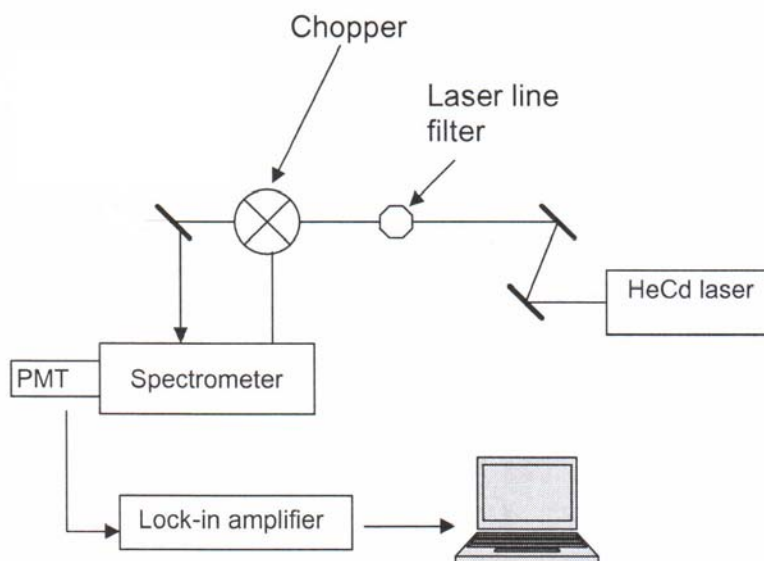
Figure 2.4 Experimental set-up for photoluminescence spectroscopy [2.2].

2.4 FOURIER TRANSFORM INFARED SPECTROSCOPY

2.4.1 INTRODUCTION

Fourier transform infrared spectroscopy (FTIR) is the preferred method of infrared spectroscopy. It is a non-destructive technique that is easy to perform and provides a precise measurement of the vibrational motion of polyatomic molecules. In polyatomic molecules, the frequencies of molecular vibrations can be used to identify the various types of bonds and functional groups present in the molecule. The frequencies of these molecular vibrations usually lie in the infrared region of the electromagnetic spectrum. For infrared spectroscopy, the electric dipole moment of the molecule must change during vibration in order for a particular vibrational mode to be infrared active. The vibrations of some molecules are thus sensitive to changes of the charge on the compounds. FTIR has been identified as the technique of choice

to gain qualitative insight into the non-photoinduced charge transfer mechanism and hence transformation in the chemical structure of rr-P3HT when blended with PCBM.

2.4.2 THEORY

In infrared spectroscopy, infrared radiation is passed through a sample where some of the radiation is absorbed by the sample and some of it is passed through (transmitted). The resulting spectrum represents the molecular absorption and transmission, creating a spectral fingerprint of the sample, since no two unique structures produce the same infrared spectrum.

FTIR spectroscopy utilises an optical device called a Michelson interferometer, as depicted in Figure 2.5. It uses a method that measures all of the infrared frequencies simultaneously, rather than individually; in order to overcome the slow scanning speeds of older dispersion infrared instruments. The interferometer employs a beamsplitter that takes the incoming infrared beam and divides it into two optical beams. One beam reflects off a flat mirror that is fixed and the other beam reflects off a flat mirror which is mounted on a mechanism that allows the mirror to move a short distance away from the beamsplitter. The two beams thus reflect off their respective mirrors and are recombined when they meet back at the beamsplitter. Since the path that one beam travels is a fixed length and the other is constantly changing as its mirror moves, the signal which exits the interferometer is the result of these two beams interfering with each other. The path length difference, or retardation d, is in effect caused by the displacement of the moving mirror. The resulting signal is called an interferogram, which has the unique property that every data point (a function of the moving mirror position) that makes up the signal, has information about every

infrared frequency that comes from the source. Since the measured interferogram signal cannot be measured directly, a means of decoding the individual frequencies is accomplished by using the Fourier transformation mathematical technique via computer code, which presents the user with the desired spectral information for analysis.
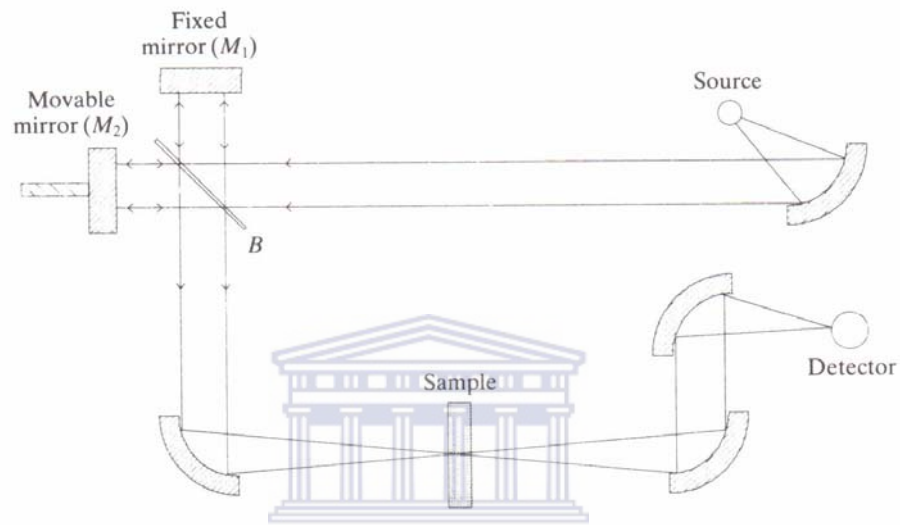
Figure 2.5   Typical layout of a Michelson interferometer utilised an FTIR spectrometer [2.3].

For infrared spectroscopy, the term wavenumber ω or 'frequency' in units of cm^{-1} is used rather than the wavelength λ, where:

$$\omega = \frac{1}{\lambda} \qquad\qquad (2.5)$$

If the spectrum that is measured is in the frequency range 1 to ∞ cm^{-1}, then the path difference will be δ, while the intensity of the radiation, B(ω), is a function of the frequency of the spectrum. The amplitude of the interferogram, I(δ), is given by the

superposition of the two beams with equal intensities. The variation of intensity is a function of difference in path-length, which is represented by the spectrum, while the variation in power density as a function of difference in path-length is represented by an interference pattern; given by [2.4]:

$$I(\delta) = \int_{+\infty}^{-\infty} B(\omega) \cos 2\pi\omega\delta d\omega \qquad (2.6)$$

Fourier transformation allows the variation in intensity to be converted into the variation in power density, and vice versa by the Fourier transform of equation (2.6), as shown by equation (2.7):
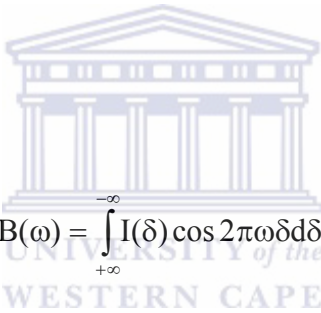
$$B(\omega) = \int_{+\infty}^{-\infty} I(\delta) \cos 2\pi\omega\delta d\delta \qquad (2.7)$$

Since it is impossible to have an infinite number of data points and to have the path difference approach to infinity, the problem can best be approached by having an optimum number of data points for a given required resolution. In general there are N data points available that can be taken in the spectral range between ω_{max} and ω_{min}, in equal intervals of retardation h. The number of points required, N, is given by [2.4]:

$$N = \frac{2(\omega_{max} - \omega_{min})}{\Delta\omega} \qquad (2.8)$$

41

since h is defined as:

$$2h = \frac{1}{\omega_{max} - \omega_{min}}$$

(2.9)

Furthermore, it can be shown from equation (2.2) that the absorption coefficient $\alpha(\omega)$, defined as the amount of radiation absorbed per unit thickness, is related to the transmission spectrum by:

$$\alpha(\omega) = -\frac{\ln[T(\omega)]}{d}$$

(2.10)

where d is the thickness of the active rr-P3HT:PCBM layer.
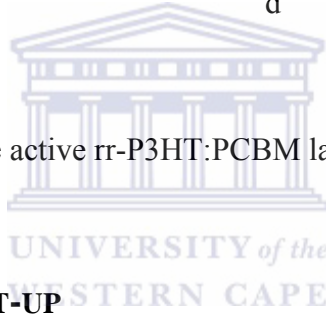
2.4.3 EXPERIMENTAL SET-UP

FTIR absorption spectra were collected in transmission geometry from 400 – 4000 cm^{-1} with a spectral resolution of 1 cm^{-1}, using a Perkin-Elmer Spectrum 100 FTIR spectrophotometer (National Centre for Nano-Structured Materials, Council for Scientific and Industrial Research). Unlike glasses, semiconductors like silicon have good infrared transparency and are not sensitive to humidity. Hence the substrate chosen for the characterization of thin films are mono-crystalline silicon (c-Si) wafers of orientation <100>. Infrared transmission $T(\omega)$ as a function of vibrational frequency ω was measured by first collecting a background spectrum of the c-Si substrate to eliminate absorption by the c-Si substrate. The sample (thin film layer on

c-Si substrate) was subsequently measured and the spectrum of the thin film produced.

2.5 RAMAN SPECTROSCOPY

2.5.1 INTRODUCTION

Raman spectroscopy is the study of the chemical structure and physical form of a molecule, identification of substances from characteristic spectral patterns and quantitative determination of the amount of a substance in a sample. The underlying process of Raman spectroscopy is Raman scattering, during which monochromatic radiation, used to irradiate the sample, is scattered from the molecule, one vibrational unit of energy different from the incident beam. This unit of energy, which is characteristic of the scattering molecule then gets detected and measured; thus allowing for the identification of the vibrations of a molecule. In this study Raman spectroscopy will be employed as a complementary technique to probe specific changes in the chemical structure of rr-P3HT and its blends with PCBM.

2.5.2 THEORY

2.5.2.1 Scattering of a Light Wave by a Molecule

When radiation interacts with matter, one of two processes can occur, namely scattering or absorption. Scattered radiation is released when the light wave, which can be considered as an oscillating dipole, transfers its energy to the molecule, subsequently distorting (polarising) the electrons around the nuclei of the molecule

causing it to go to a higher energy state. This interaction can be considered as the formation of a complex between the light energy and the electrons in which the nuclei of the molecule do not have enough time to move appreciably. This complex is not stable, resulting in the light being released almost immediately as scattered radiation [2.5].

This process differs from light absorption in the following ways:

- The additional light energy does not promote an electron to a higher energy state of the molecule. Instead all states of the molecule are involved to different extents and are mixed to form states of the distorted complex.

- The lifetime of the excited state is very short compared to most absorption processes and the radiation is scattered as a sphere and is not lost by energy transfer within the molecule or emitted at a lower energy.

Two types of scattering exist. The most intense form is Rayleigh scattering, which occurs when the electron cloud relaxes without any nuclear movement. This process is essentially elastic, since no appreciable change in energy of the molecule is observed. On the other hand, Raman scattering, which is a much infrequent event as compared to Rayleigh scattering, occurs when the light and the electrons interact and the nuclei begin to move at the same time. Since the nuclei are much heavier than the electrons, there is an appreciable change in energy of the molecule to a lower or higher energy, depending on whether the electron was initially in the ground state or in a vibrationally excited state. When the molecule is initially in the ground state the process is known as Stokes scattering, whereas when the molecule starts off in an

excited state, anti-Stokes scattering occurs. Figure 2.6 shows these two scattering processes compared to Rayleigh scattering.
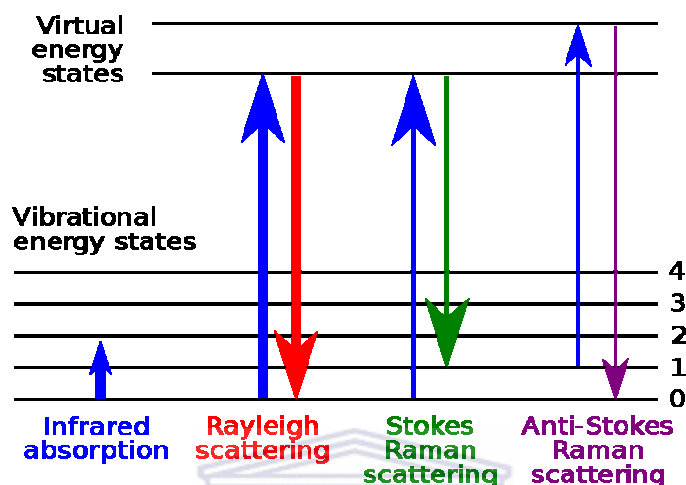

Figure 2.6   Diagram of the Rayleigh and Raman scattering processes.

Rayleigh scattering will be the most intense process since most photons scatter in this manner. Usually Raman scattering is only recorded on the low-energy side to give Stokes scattering, since this signal is much more intense than the anti-Stokes scattering signal. This is due to the fact that a minimal amount of molecules are in the excited state at room temperature.

2.5.2.2 Hooke's Law

Hooke's law provides the relationship between the frequency, mass of the atoms involved in the vibration and the bond strength for a diatomic molecule by (see Appendix):

$$v = \frac{1}{2\pi}\sqrt{\frac{K}{\mu}}$$

(2.11)

45

where ν is the frequency, K is force constant of the bond between atoms A and B, and μ the reduced mass of A and B with masses M_A and M_B. The reduced mass μ is given by:

$$\mu = \frac{M_A M_B}{M_A + M_B} \qquad (2.12)$$

Hooke's law allows for easy approximations of the order of energies of specific vibrations: the lighter the atoms, the higher the frequency will be and vice versa. The force constant, K is a measure of the bond strength, thus the stronger the bond the higher the measured frequency.

**2.5.2.3 Selection Rules for Raman Scattering**

Provided there is no change in its electronic energy, the energy of a molecule can be divided into a number of degrees of freedom. Three of these are taken up to describe the translation of the molecule in space and a further three to describe rotational movement. However, for linear molecules; i.e. two atoms bonded at an angle of 180°, only two types of rotation are possible. The molecule can either rotate around the axis or about it. Hence, for a molecule consisting of N atoms the number of vibrational degrees of freedom will be 3N – 6, and 3N – 5 for linear molecules.

For example, a diatomic molecule such as oxygen only has one vibration, which is a stretch of the O=O bond. This stretch will change the polarizability of the molecule. Intense Raman scattering occurs from vibrations that cause a change in the polarizability of the electron cloud of the molecule [2.5]. The change in polarizability

causes the movement of the nuclei, which creates Stokes and anti-Stokes scattering. Generally the symmetrical stretch causes large polarization changes and hence strong Raman scattering, whereas the asymmetric stretches cause dipole changes, which leads to intense infrared absorption. Mathematically the change in polarizability involves the change of a dipole, μ in the Cartesian directions, given by [2.5]:

$$\mu = \alpha E \qquad (2.13)$$

where α is the polarizability of the electron cloud of the molecule and E the electric field of the incident photon. Usually α is labelled according to its components, e.g. α_{xx} where the first subscript refers to the direction of the polarizability of the molecule and the second refers to the polarization of the incident light. Therefore:
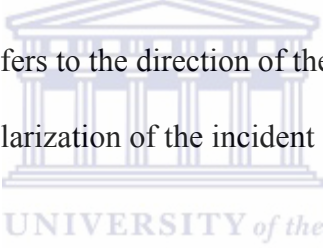
$$\mu_x = \alpha_{xx} E_x + \alpha_{xy} E_y + \alpha_{xz} E_z \qquad (2.14)$$

Similar expressions exist for μ_y and μ_z. Finally, the intensity of the beam scattered during Raman scattering, I, is given by:

$$I = K\ell\alpha^2\omega^4 \qquad (2.15)$$

where K consists of constants such as the speed of light, ℓ is the laser power, α the polarizability of the electrons in the molecule, and ω the frequency of the incident radiation.

2.5.3 EXPERIMENTAL SET-UP

Figure 2.7 shows a typical set-up for Raman spectroscopy. A monochromatic visible laser is used as the excitation source. The laser is passed through a pinhole, measured by a spectrometer and then collected as an expanded parallel beam. This is done in order to fill the optics of the microscope. The radiation is then deflected by mirrors towards the notch filter, which reflects the light into the microscope. After interaction of the light with the sample, the scattered radiation is collected from the microscope back through the same optics. The scattered radiation then passes through the notch filter at an angle that allows transmission of the scattered radiation. This radiation is then passed through a grating and onto the charge coupled device (CCD) detector.

A Jobin-Yvon HR800 micro-Raman spectrometer (National Centre for Nano-Structured Materials, Council for Scientific and Industrial Research) was used during our investigation. The Raman spectra were collected in backscattering geometry at room temperature in the region $100 - 3000 \text{ cm}^{-1}$ with a spectral resolution of 0.4 cm^{-1}, using a 514.5 nm Ar^+ excitation laser.
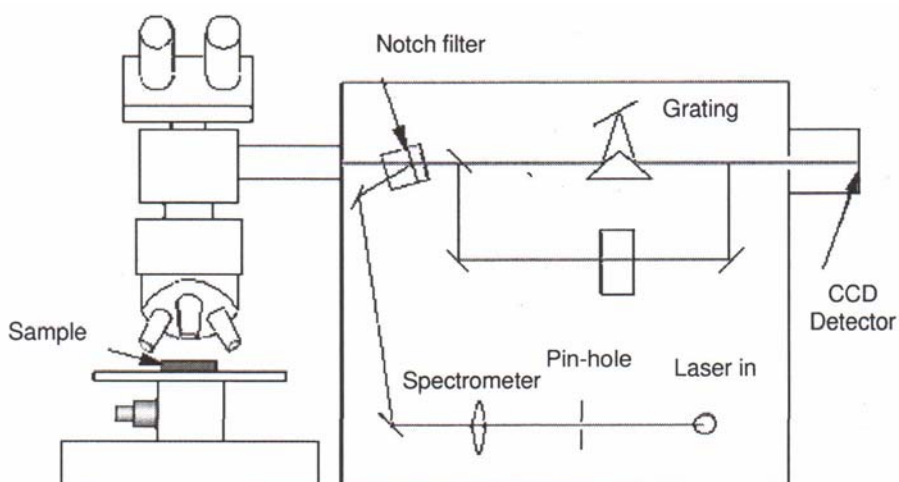

Figure 2.7   Typical set-up for Raman spectroscopy [2.5].

2.6 X-RAY DIFFRACTION

2.6.1 INTRODUCTION

X-ray diffraction (XRD) can reveal the microscopic and the morphological structure of thin films. X-rays are electromagnetic radiation similar to light, but with much smaller wavelength. X-rays are generated by an X-ray tube, a vacuum tube that uses a high voltage to accelerate the electrons released by a hot cathode to a high velocity. The high velocity electrons collide with a metal target, the anode, creating the X-rays When the electrons hit the target, X-rays are created by two different atomic processes:
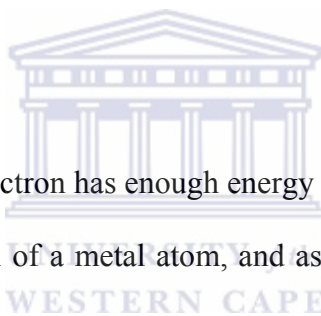
X-ray fluorescence: If the electron has enough energy it can knock an orbital electron out of the inner electron shell of a metal atom, and as a result electrons from higher energy levels then fill up the vacancy and X-ray photons are emitted. This process produces an emission spectrum of X-ray frequencies, sometimes referred to as the spectral lines. Usually these are transitions from upper shells into K shell (called K lines), into L shell (called L lines).

Bremsstrahlung: This is radiation given off by the electrons as they are scattered by the strong electric field near the high-*Z* (proton number) nuclei. These X-rays have a continuous spectrum.

Diffraction is a phenomenon that occurs when waves interfere with a structure whose repeat distance is about the same as that of the incident wavelength. Upon interaction constructive and destructive interference patterns result due to the scattering of the incoming wave fronts by the structure. The wavelength range of x-rays is about the same as that of the inter-atomic spacing found in three-dimensional crystalline structures, meaning that x-rays can be diffracted by these crystalline structures with each atom in the crystalline structure serving as a scattering centre for the incoming wave fronts. This phenomenon is known as x-ray diffraction (XRD) and can be used as a tool for the investigation of the fine, crystalline structure of matter. Most important for the purpose of this study are the identification of any crystalline phases present and the determination of interlayer spacing d in the rr-P3HT film and its blend with PCBM. It can also determine the orientation of the crystal grains in the thin film. The film could also be shown to be polycrystalline, single crystal or amorphous.
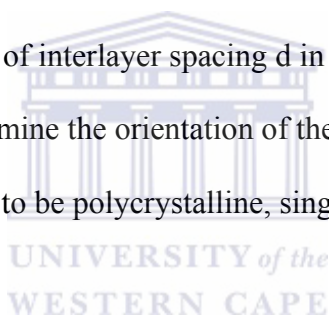
2.6.2 THEORY

2.6.2.1 Crystal Structure and Bravais Lattices

The atoms found in materials can be either randomly distributed, thus making the material amorphous or they can be arranged in a periodic pattern in three dimensions, resulting in the material being crystalline. When thinking about the atomic arrangement within a crystal, it is best to imagine the atoms as a set of imaginary points with a fixed relation in space.

Figure 2.8 illustrates the above concept, referred to as a point lattice and is defined as an array of points in space, so arranged that each point have identical surroundings.
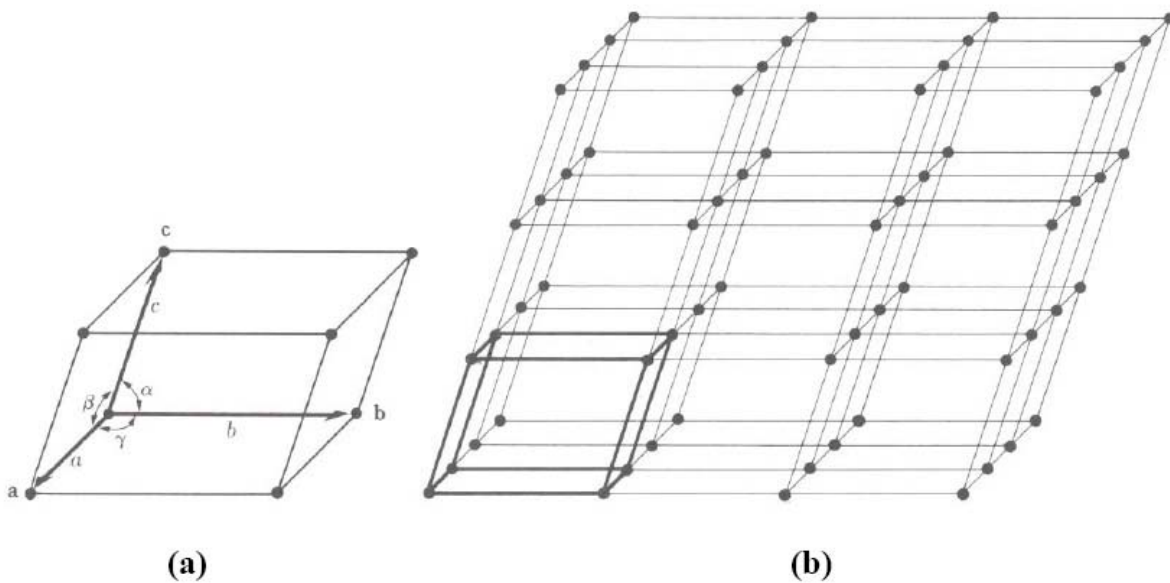
Figure 2.8   Schematic of: (a) primitive cell and the angles between the translation vectors and (b) its point lattice [2.6].

By drawing three vectors **a**, **b** and **c** from the corner of any lattice point, one generates a point lattice unit cell. These vectors, known as the crystallographic axes of the unit cell can also be described in terms of their lengths (a, b and c) and the angle between them (α, β and γ), known as the lattice constants or lattice parameters as shown in Figure 2.8. Not only do the crystallographic axes define the unit cell, but it also defines the whole point lattice, which can be produced by repeated action of the vectors. Depending on the relationship between the lattice parameters (i.e. a, b, c, α, β and γ) one can distinguish between fourteen different point or Bravais lattices, as described in Table 2.2.

The direction of any vector within the Bravais lattice is given as a linear combination of the three crystallographic axes as:

$$\mathbf{x} = u\mathbf{a} + v\mathbf{b} + w\mathbf{c} \qquad (2.16)$$

where $\mathbf{a}$, $\mathbf{b}$ or $\mathbf{c}$ is any vector in the Bravais lattice and u, v and w are the coordinates of any point on the vector

In short, equation (2.16) can be written as [u v w] as shown in Figure 2.9. Furthermore, [u v w] are always converted to a set of smallest integers, e.g. [2 2 4] and [½½1] represents the same direction, with [1 1 2] the preferred notation. Collectively, all of these vectors form the reciprocal space of the lattice, or reciprocal lattice.
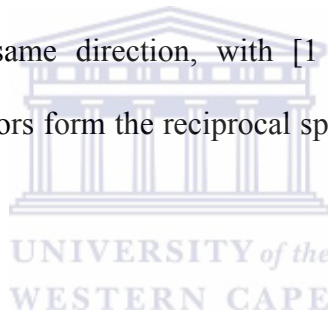
Table 2.2   Description of the fourteen Bravais lattices [2.6].

	Axial length and angles	Bravais lattice	Lattice symbol
Cubic	Three equal axis at right angles $a = b = c,\ \alpha = \beta = \gamma = 90°$	Simple Body-centered Face-centered	P I F
Tetragonal	Three angles at right angles, two equal $a = b \neq c,\ \alpha = \beta = \gamma = 90°$	Simple Body-centered	P I
Orthorhombic	Three unequal axes at right angles $a \neq b \neq c,\ \alpha = \beta = \gamma = 90°$	Simple Body-centered Face-centered Base-centered	P I F C
Rhombohedral	Three equal axes, equally inclined $a = b = c,\ \alpha = \beta = \gamma \neq 90°$	Simple	R
Hexagonal	Two equal co-planar axes at 120°, third axis at right angles $a = b \neq c,\ \alpha = \beta = 90°\ \gamma = 120°$	Simple	P
Monoclinic	Three unequal axes, one pair not at right angles $a \neq b \neq c,\ \alpha = \gamma = 90° \neq \beta$	Simple Base-centered	P C
Triclinic	Three unequal axes, unequally inclined and none at right angles $a \neq b \neq c,\ \alpha \neq \beta \neq \gamma \neq 90°$	Simple	P

Given any Bravais lattice, a lattice plane is defined as any plane containing at least three non-collinear lattice points. A family of lattice planes is a set of parallel planes, which together contain all the points of the three-dimensional Bravais lattice. For

53

cubic systems, there is an intrinsic relationship between the family of lattice planes
and the vectors in the reciprocal lattice, which provides a convenient way of
specifying the orientation of the lattice planes in space.

Generally for cubic systems, the orientation of a plane is given by the vector normal
to it and is denoted by Miller indices, h k l, contained in round brackets, e.g. (h k l). In
Figure 2.9 the vector $\vec{n} = \dfrac{\vec{a}_1}{h} + \dfrac{\vec{a}_2}{k} + \dfrac{\vec{a}_3}{l}$ is normal to the plane (h k l) that intercepts the

unit cell at $\dfrac{\vec{a}_1}{h} + \dfrac{\vec{a}_2}{k} + \dfrac{\vec{a}_3}{l}$, where $\mathbf{a}_1$, $\mathbf{a}_2$ and $\mathbf{a}_3$ are the crystallographic axes. Similar to

lattice vectors, planes related by symmetry are called planes of a form and is denoted
by {h k l}.
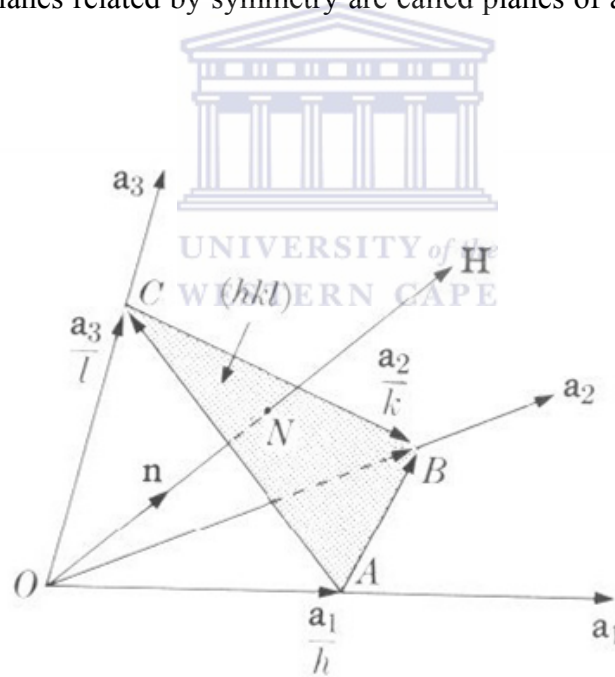
Figure 2.9   Relationship between the reciprocal lattice vector and the crystal plane

(*h k l*).

2.6.2.2 Bragg's Law of Diffraction

The basis for x-ray diffraction is described by the Bragg's equation. He discovered that diffraction could be pictured as a reflection of the incident beam from the lattice planes. Bragg subsequently developed a mathematical equation for the condition of reflection, which is equivalent to simultaneously solving the three Laue equations but provides for a simpler and more workable expression of diffraction [2.6].

Consider a beam of parallel X-rays penetrating a stack of planes of spacing d, at a glancing angle θ as depicted in the following Figure 2.10. Each plane must be pictured as reflecting a fraction of the incident beam.
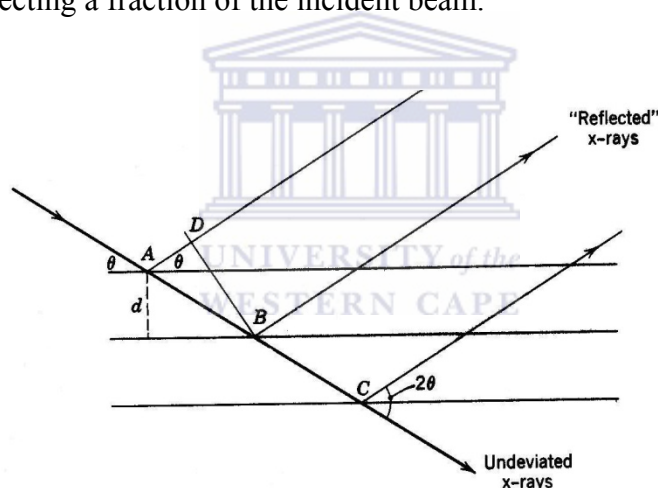

Figure 2.10 The condition of reflection – Bragg's law.

The reflected rays combine to form a diffracted beam if they happen to be in phase by a whole number of wavelengths – that is, if their path difference AB – AD = $n\lambda$, where n = 1, 2, 3.

AB and AD is given by:

$$AB = \frac{d}{\sin\theta}$$

$$AD = AB\cos 2\theta = \frac{d}{\sin\theta}(\cos 2\theta)$$

Therefore:

$$n\lambda = \frac{d}{\sin\theta} - \frac{d}{\sin\theta}(\cos 2\theta) = \frac{d}{\sin\theta}(1 - \cos 2\theta) = \frac{d}{\sin\theta}(2\sin\theta^2\theta)$$

$$\therefore n\lambda = 2d\sin\theta \qquad\qquad (2.17)$$

This is the Bragg condition for reflection. The equation gives the angle θ, at which a set of planes of spacing d cooperatively reflects X-radiation of wavelength λ in the nth order.
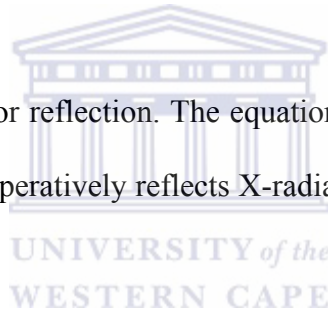
The interplanar spacing d, of a set of parallel crystallographic lattice planes, is defined by the dimensions of the crystal unit cell. There exist an infinite number of such families of parallel planes in a given crystalline lattice, and each is associated with a particular Bragg angle θ, as indicated in Figure 2.10. Each set of planes is characterized by the three indices *hkl*, and the resultant diffracted beam is termed the *hkl*-reflection.

2.6.3 EXPERIMENTAL SET-UP

Typical instrumentation consists of three basic parts:

- A source of radiation, consisting of an X-ray tube and a high voltage generator

- The diffractometer

- The detector equipment.

The Bragg-Brentano geometry, also known as the $\theta-2\theta$ geometry, usually employed for powder samples, is also commonly used to determine which, if any, of a film's diffraction planes lie parallel to the substrate surface. Figure 2.11 depicts the geometry for Bragg-Brentano measurements.
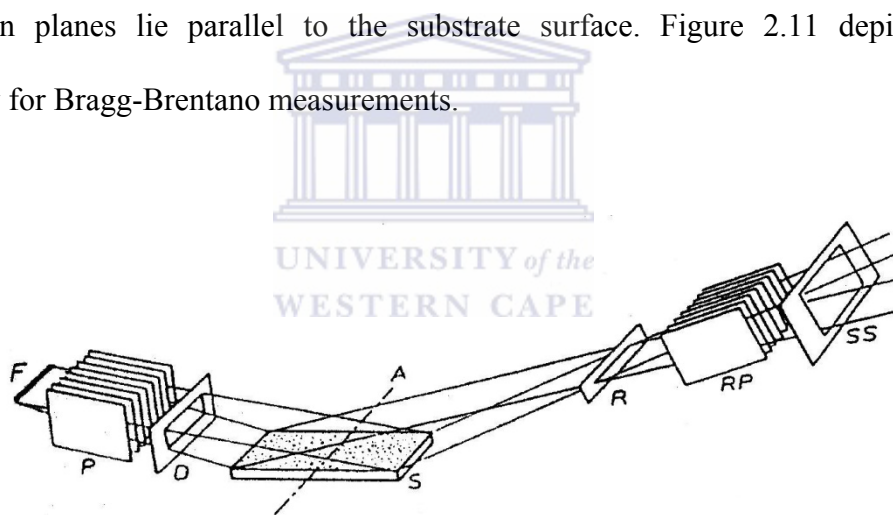
Figure 2.11   The Bragg-Brentano geometry. X-rays from a line source F falls onto a specimen S, undergoes diffraction and pass through slit R into the detector. The detector and the tube, rotate around the axis A to ensure diffraction through 2θ [2.6].

X-ray diffraction (XRD) spectra were collected with a Bragg-Brentano geometry with 2θ-values ranging from $3 - 40°$, with a step size of $0.02°$, using a PANalytical® X-ray

powder diffractometer operating at 45 kV and 40 mA (National Centre for Nano-Structured Materials, Council for Scientific and Industrial Research). Monochromatic Copper (Cu) Kα_1 radiation with a wavelength of 0.154 nm was used as the X-ray source. The system also includes divergence slits on the tube side and anti-scattering slits on the detector side. A filter is placed in the diffracted beam-path to suppress the K radiation and to decrease the background radiation originating in the specimen.

2.7 TRANSMISSION ELECTRON MICROSCOPY

2.7.1 INTRODUCTION

The electron microscope utilizes an electron beam that is focused by an assembly of electromagnetic lenses, with the beam only enclosed in an evacuated column. It is an improvement of the light microscope especially as far as resolution is concerned since electrons have much shorter wavelengths (in the range of 10ths of pm depending on the accelerating voltage between the cathode and anode in the electron gun) than light, which is of the order five times longer [2.7, 2.8]. High-resolution transmission electron microscopy (HR-TEM) was employed to examine the internal structure and crystallinity of rr-P3HT and its blends with PCBM.

2.7.2 BASIC OPERATION

A basic TEM consists of an electron gun which provides the illumination, a series of electromagnetic lenses, a viewing screen coated with a layer of electron-fluorescent material, and a camera which must work in the vacuum within the microscope. These components are assembled into a vertical 'microscope column'. A typical example is

shown in Figure 2.12. The electron gun emits a diverging beam of electrons through the anode aperture. This beam can be deflected to be aligned parallel to the optical axis of the lens system. The deflector coils are controlled by the gun alignment controls, and the electron beam is focused down to a fairly small spot by the first condenser lens. The setting of this lens controls the ultimate spot size attainable by the condenser system, which is generally less than 1 μm. The second condenser lens projects the beam at the specimen in such a way that the area illuminated and the convergence angle can be controlled. Below this lens is a moveable aperture that selects the primary beam and cut out any scattered beams, thus giving a clear diffraction image. The best resolution and image sharpness is obtained by working with the smallest condenser lens aperture (<300 μm) while exiting the second condenser lens more strongly. However, this reduces the illumination level considerably.
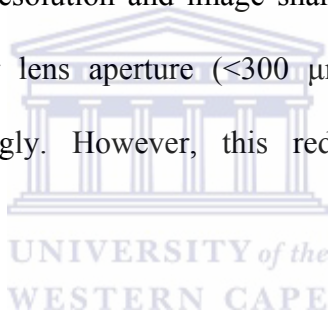
The condenser stigmator placed below the condenser aperture compensates for astigmatism in the illumination system. In this same region are the 'wobbler' coils for aiding focusing and two sets of alignment coils in order to bring the beam exactly onto the optical axis in the crucial part of the microscope near the specimen. The specimen, objective aperture and objective stigmator coils are all placed inside the objective lens windings. The objective lens focuses on the specimen and forms an intermediate image at a magnification of about 50X. The objective aperture sits in the 'back focal plane' of the objective lens and enables the operator to allow particular groups of electrons to contribute to the final image. In the plane of the first intermediate image is the 'selected area' aperture, which allows a particular part of the image to be selected for examination and diffraction analysis. Below this aperture are

three or four lenses whose function is to magnify the image or diffraction pattern and project in into the fluorescent screen.

The electronics needed to control the electron gun, six or seven lenses and a vacuum system is quite complex. For this reason there is a tendency for modern electron microscopes to be controlled by a built-in computer, which results in a reduction in the number of manual controls.
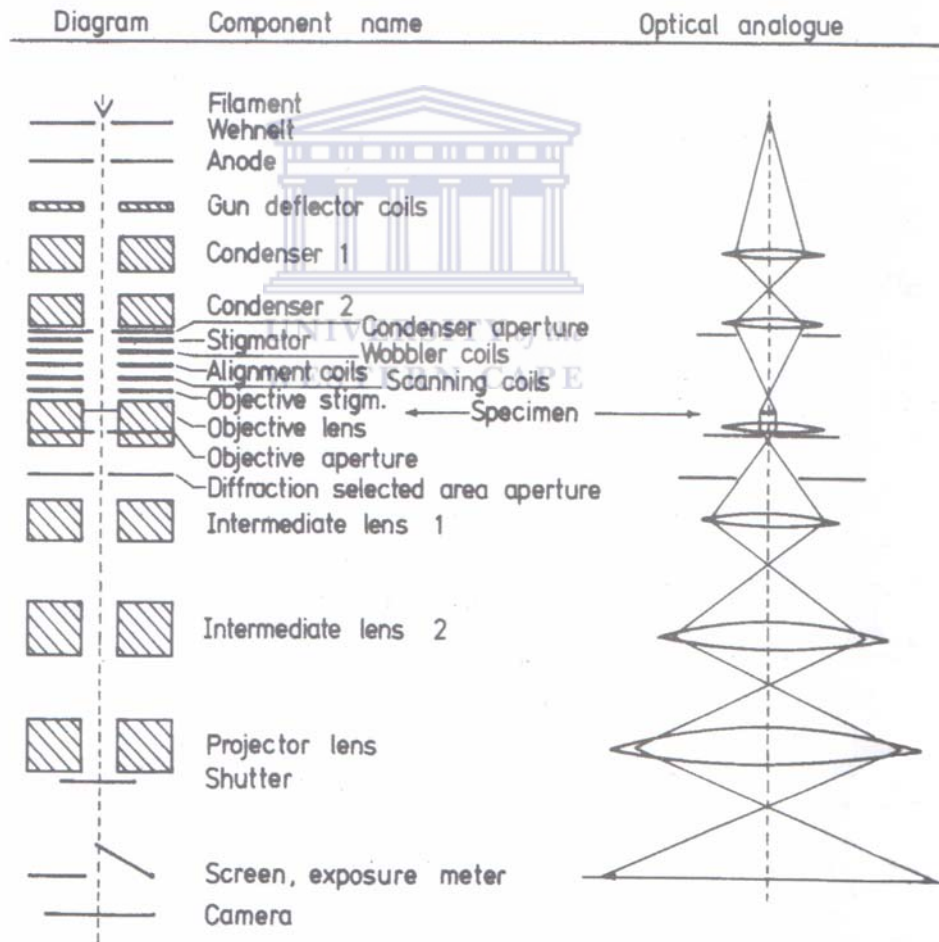

Figure 2.12   A cross-section of the basic components of HR-TEM. The optical analogue is also provided.

2.7.3 ELECTRON DIFFRACTION

In all microscopes a diffraction pattern of crystalline specimens inevitably forms in the back focal plane of the objective lens. In this plane all parallel 'rays' leaving the specimen in a specific direction pass through a point in the 'diffraction pattern'.

During normal imaging the diffraction pattern is unseen because the first intermediate lens is focused on the first intermediate image (bottom of Figure 2.12) and this is what is finally projected onto the screen. In diffraction mode the first intermediate lens is de-excited so that it 'sees' the diffraction pattern in the back focal plane of the objective lens and projects magnified versions of this pattern instead to the projector system. There are two fundamentally different ways of examining the diffraction pattern from a selected area of the specimen. In the selected area diffraction technique a small area of the specimen is selected, although a larger area is being illuminated. In the alternative micro-diffraction technique the beam is condensed into a small spot so that the diffraction pattern comes from the whole of the (small) illuminated area. In this case the diameter selected on the specimen is the same as the diameter of the beam at the specimen. This is the only way to obtain a diffraction pattern from a region smaller than 1 μm in diameter (down to a few nanometers). A diffraction pattern is obtained when the electron beam encounters crystalline material, resulting in strong preferential scattering in certain well-defined directions governed by the Bragg's Law in equation (2.17).

The Bragg condition is said to be satisfied when a crystal is orientated in such a way that the incident electron-beam satisfy the diffraction angle for the specific plane. Since most of the diffracted electrons are concentrated in these Bragg directions, a

crystal grain will appear bright if the diffracted beams pass through the objective aperture and dark if stopped by the objective aperture. Thus, in a polycrystalline material some grains will appear bright and some dark, depending on their orientation with respect to the electron beam (see for example Figure 2.13(b)). Different types of diffraction pattern arise from different specimen microstructure as can be seen in Figure 2.13(a) shows a single crystal (i.e. a specimen consisting of a single repeating array of atoms) orientated in such a way that several sets of planes are parallel to the beam. This gives rise to a diffraction pattern consisting of a regular array of bright spots. The arrangement of these spots depends upon the orientation of the atomic planes in the electron microscope. If the specimen contains several crystals of different orientations as in Figure 2.13(b), then the diffraction pattern is the sum of the individual patterns. The spots are not randomly distributed, but tend to fall on rings of constant radii.
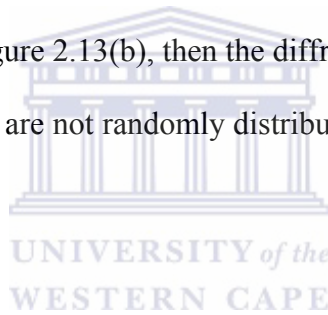
If the specimen consists of a large number of small crystallites (grains) of similar crystal structure, but at different orientations to one another (i.e. a polycrystal as in Figure 2.13(c)) the diffraction pattern will consist of a series of sharp concentric rings. It can easily be seen that this pattern evolves from a large number of single crystal diffraction patterns, each rotated by a small amount with respect to one another. In the case of an amorphous material, the constituent atoms are arranged entirely randomly and without any distinct repeating structure. For such materials the diffraction pattern will contain no discrete maxima. It rather consists of diffuse diffraction rings around the bright central spot of unscattered electrons.
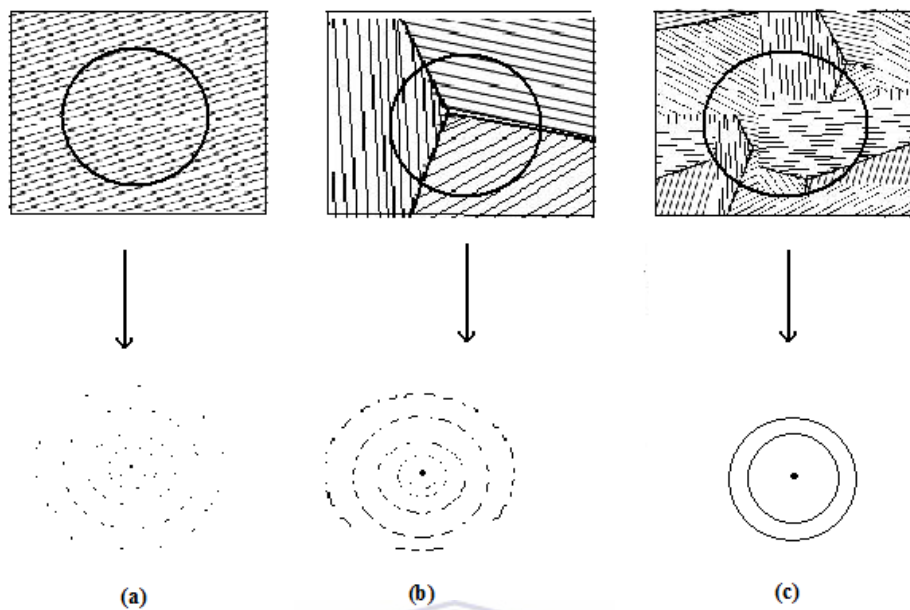
Figure 2.13   Types of diffraction pattern which arise from different specimen microstructure: (a) A single perfect crystal, (b) A small number of grains – notice that even with three grain spots begin to form circles, (c) A large number of randomly orientated grains, the spots have now merged into rings.

Using the standard Miller index notation [2.9] to define plane and directions in the crystal, diffraction patterns can be interpreted. Using this notation for a cubic crystal for example the interplaner spacing of planes of the type (*hkl*) is given by:

$$d_{hkl} = \frac{a}{\sqrt{h^2 + k^2 + l^2}} \qquad (2.18)$$

where a is the lattice parameter of the unit cell and h, k and *l* the Miller indices. For

first order diffraction i.e. n =1, Bragg's law reduces to:

$$\lambda = 2d \sin \theta \qquad (2.19)$$

For small angles of θ, which if typical of electron diffraction, we can write sin θ = θ,

and equation (2.19) further reduces to:

$$\lambda = 2d\theta \qquad (2.20)$$

Consider now a beam of electrons impinging on a crystalline specimen as in Figure

2.14. Some of the electrons pass through the specimen without interaction and hit the

screen or film, which is a distance L from the specimen, at O. Other electrons are

diffracted through an angle θ by the crystal planes of spacing d, and these electrons hit

the film at A, which is a distance r from 0. From simple geometry, it can be seen that

for small angles of diffraction:

$$\frac{r}{L} = 2\theta \qquad (2.21)$$

Combining equations (2.20) and (2.21), we find:

$$rd = L\lambda \qquad (2.22)$$

λL is called the camera constant and is determined by analysing a known crystal.

From equation (2.22) it can be seen that the distance of a diffraction spot from the

undiffracted spot, r, is therefore inversely proportional to the d spacing of the diffracting planes. A table of the $\lambda L/d_{hkl}$ values for different (*hkl*) planes can be drawn up. By measuring r directly in the pattern in the pattern on the photographic plate and comparing it with the values in the table, the pattern can be indexed, i.e. the respective h, k and *l* values can be determined.
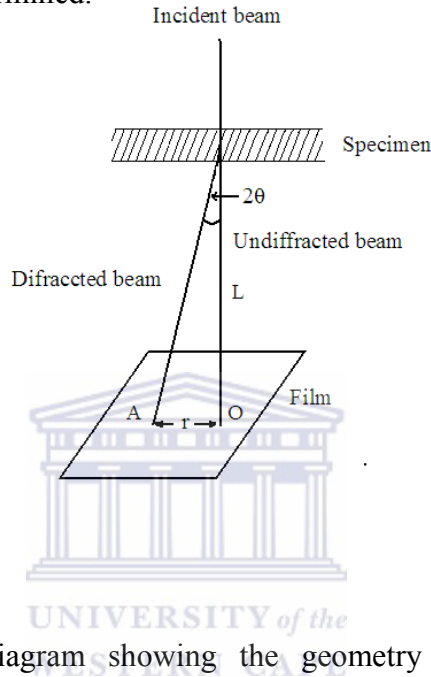
Figure 2.14   Schematic diagram showing the geometry of diffraction pattern
formation

An alternative method for indexing diffraction patterns involves determining the ratio between the magnitudes of two diffraction vectors as defined in the reciprocal lattice theory [2.9]. According to the theory for a face centred cubic (F.C.C.) crystal as an example, the diffraction vector g_{hkl} is a reciprocal lattice vector such that d is given as in equation (2.18). The ratio between:

$$\frac{|g_{h1k1l1}|}{|g_{h2k2l2}|} = r_{hkl} = \frac{1}{d_{hkl}} \qquad (2.23)$$

65

The magnitude of two diffraction vectors on the photographic plate is therefore equivalent to the ratio between the magnitudes of the corresponding reciprocal lattice vectors, i.e.

$$\frac{|g_{h1k1l1}|}{|g_{h2k2l2}|} = \frac{r_{h1k1l1}}{r_{h2k2l2}} = \frac{d_{h1k1l1}}{d_{h1k1l1}} = \frac{\sqrt{h_1^2 + k_1^2 + l_1^2}}{\sqrt{h_2^2 + k_2^2 + l_2^2}} \qquad (2.24)$$

Tables can now be drawn up for the ratios between the $\sqrt{h^2 + k^2 + l^2}$ values of all the (*hkl*) planes in the crystal. In order to index the diffraction vectors $\mathbf{g}_{hkl}$, one only need to determine the distances of any two diffraction spots from the central undiffracted spot on the photographic plate. By comparing the calculated values with those in the table, the respective (*hkl*) indices can be assigned. Once two spots have been indexed the whole diffraction pattern can be indexed by superposition.
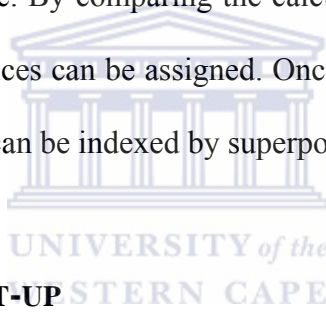
2.7.4 EXPERIMENTAL SET-UP

The work was done on a FEI Tecnai F20 field emission high-resolution electron microscope (HR-TEM) located at the University of Western Cape (UWC) in the Electron Microscope Unit, operated at 120 kV capable of obtaining a resolution of about 0.1 nm. Throughout the investigation the first condenser lens was set to the best workable spot size, which was about 1 μm. An objective lens moveable aperture of between 20 μm and 80 μm in diameter was employed and during selected area diffraction a 10 to 30 μm diameter field limiting aperture was inserted. Specimens for HR-TEM analysis were prepared by transferring a small drop of each solution of rr-P3HT and its blends with PCBM on a holey-carbon copper grid and dried at ambient conditions.

REFERENCES

[2.1]   R. C. Denney, R. Sinclair, in "Visible and Ultraviolet Spectroscopy", John Wiley & Sons, Reading, London (1987)

[2.2]   O. D. Pagni, in "On the MOCVD growth ZnO", PhD thesis, University of Port Elizabeth (2002)

[2.3]   C. N. Banwell, E. M. McCash, in "Fundamentals of Molecular Spectroscopy", McGraw-Hill Publishing Company, Reading, London (1994)

[2.4]   B. George, P. McIntyre, in "Infrared Spectroscopy, Analytical Chemistry by Open Learning", Wiley & Sons Ltd. (1987)

[2.5]   E. Smith, G. Dent, in "Modern Raman Spectroscopy: A practical approach", Wiley and Sons Ltd., Great Britain (2005)

[2.6]   B. D. Cullity, in "Elements of X-ray diffraction", Addison-Wesley Publishing Company, Reading, Massachusetts (1978)

[2.7]   De Broglie, Phil Mag (1924) 446

[2.8]   C. Davidson, L. H. Germer, Physical Rev. 30 (1927) 705

[2.9]   C. Hammond, in "Introduction to Crystallogrophy", Oxford University Press (1990)

CHAPTER 3

Optical Properties

3.1 INTRODUCTION

In the past decade, the focus on organic photovoltaic (OPV) devices has increased significantly and several reviews on OPVs have consequently been published [3.1-3.8]. OPVs offer low-cost, low thermal budget, solution processing, flexible processing and very high speed of processing as compared to its expensive inorganic counterparts. Various organic solar cell structures are currently being studied worldwide, with the donor/acceptor bulk heterojuction polymer solar cell being considered as the most promising approach. The structure is mostly composed of a light absorbing conjugated donor polymer and a soluble fullerene (C_{60}) derivative, typically [6,6]-phenyl-C_{61}-buyric acid methyl ester (PCBM), acting as an acceptor.

Among the conjugated polymers, regioregular poly(3-hexylthiophene) (rr-P3HT) is one of the most promising conducting polymers, due to its ease of processability, chemical stability and interesting electronic and optical properties. Recently, rr-P3HT has attracted a lot of attention as a donor material in OPVs, as it has the highest carrier mobility among the conjugated polymers and an absorption edge around 650 nm (band gap of 1.9 – 2.0 eV), combined with a high hole mobility exceeding 0.1 cm^2/Vs

[3.9]. These qualities make rr-P3HT an excellent candidate as polymer donor material in polymer photovoltaic cells [3.10, 3.11].

Crucial to the power conversion efficiency of any photovoltaic device is the optical properties of the light absorbing material. In particular, the optical band gap is the most widely studied optical property for solar cell applications, since it is related to the electronic structure of the material and, more importantly, since the efficiency of is directly related to it. In this chapter we report on the optical absorption and emission properties of spin-coated rr-P3HT:PCBM thin films. Specific emphasis will be placed on the changes induced in the optical properties of rr-P3HT by the loading of PCBM with different weight ratios.
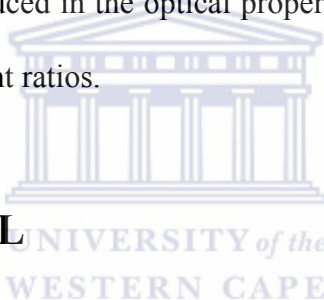
3.2 EXPERIMENTAL

3.2.1 SAMPLE PREPARATION

All chemicals were purchased from Sigma Aldrich. Regioregular P3HT (rr-P3HT) was used as the light absorbing, electron donor material, while PCBM was used as an electron acceptor material. The molecular weight of rr-P3HT reported by Sigma Aldrich was 64 000 $gmol^{-1}$, with a regularity that is greater than 98.5% for head-to-tail. These materials were used as received without any further purification.

Indium tin oxide (ITO) coated on a 1 mm-thick glass substrate, with a resistance of 8 − 12 Ω/square, and 300 μm-thick single-side polished <100> crystalline silicon (c-Si), with a resistivity of 20-30 Ωcm, were used as substrates. This allows for the execution

of various characterisation techniques. The substrates were ultrasonically cleaned with organic solvents to rid their surfaces from impurities. The cleaning sequence was as follows: 5 minutes in acetone followed by 5 minutes in methanol. The substrates were then washed in deionised water to remove any traces of the solvents and subsequently dried in ambient conditions.

For the unblended rr-P3HT and PCBM thin films; 3 mg of rr-P3HT and 3 mg of PCBM were dissolved in a 1 ml chloroform solution, respectively. For the blended samples; two mixtures of rr-P3HT and PCBM were prepared: 3 mg of rr-P3HT and PCBM with different weight (3 mg and 12 mg) were dissolved in 1 ml chloroform solution to obtain weight ratios of 1:1 and 1:4. This corresponds to a PCBM weight percentage of 50% and 80%, respectively. The solutions were stirred for 24 hours at a temperature of 50 °C to maximize mixing of the rr-P3HT:PCBM solution. Subsequently, rr-P3HT, PCBM and its blends were spin coated on the substrates. The average thickness of the resulting thin films amounted to ~ 100 nm as was measured by a Veeco Profilimeter located in the Department of Physics at UWC. The spinning rate and spin coating time were 2000 rpm and 20 seconds, respectively. Finally, the samples were dried on a hot plate at a temperature of 50 °C for 15 minutes.

3.2.2 CHARACTERISATION

Optical absorption spectra were measured from 200 – 900 nm, with a spectral resolution of 1 nm, using a Perkin-Elmer LAMDA 20 ultraviolet-visible (UV-VIS) spectrophotometer. Optical emission or photoluminescence (PL) spectra were collected at room temperature from 500 – 900 nm, with a spectral resolution of 1 nm, using a HeCd laser with an excitation wavelength of 325 nm and a power output of

13.5 mW. The thin films spin-coated on the c-Si and ITO/glass substrates and were used for PL and UV-VIS measurements, respectively.

3.3 RESULTS AND DISCUSSION

3.3.1 ABSORPTION PROPERTIES

The normalized UV-VIS absorption spectra of the thin films of rr-P3HT, PCBM and different blends of rr-P3HT:PCBM are shown in Figure 3.1. The absorption spectrum of the pure rr-P3HT thin film show two peaks at 522 nm and 547 nm and one shoulder at 589 nm. These bands can be attributed to the $\pi \rightarrow \pi^*$ transition and are similar to the reported values for rr-P3HT [3.12, 3.13]. The optical band gap of rr-P3HT, estimated from the absorption band edge, amounts to ~ 1.90 eV.
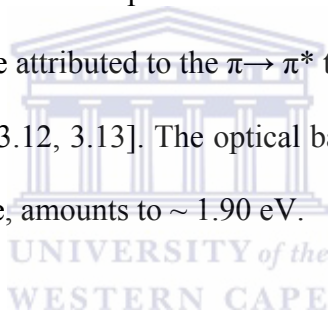
Blending rr-P3HT with an equal PCBM weight ratio yields a maximum absorption wavelength at ~ 507 nm with shoulders at ~ 474 nm and 587 nm. Interesting results are obtained when a higher weight percentage of PCBM blended with the polymer. The characteristic absorption wavelength (λ_{max}) for the film with rr-P3HT:PCBM = 1:4 appears at 435 nm. Thus, blending the polymer with increasing amounts of PCBM results in a blue shift in the characteristic absorption peak. Table 3.1 tabulates the characteristic absorption wavelength for rr-P3HT and its blends and also the degree of blue shift relative to the pure rr-P3HT film.

71
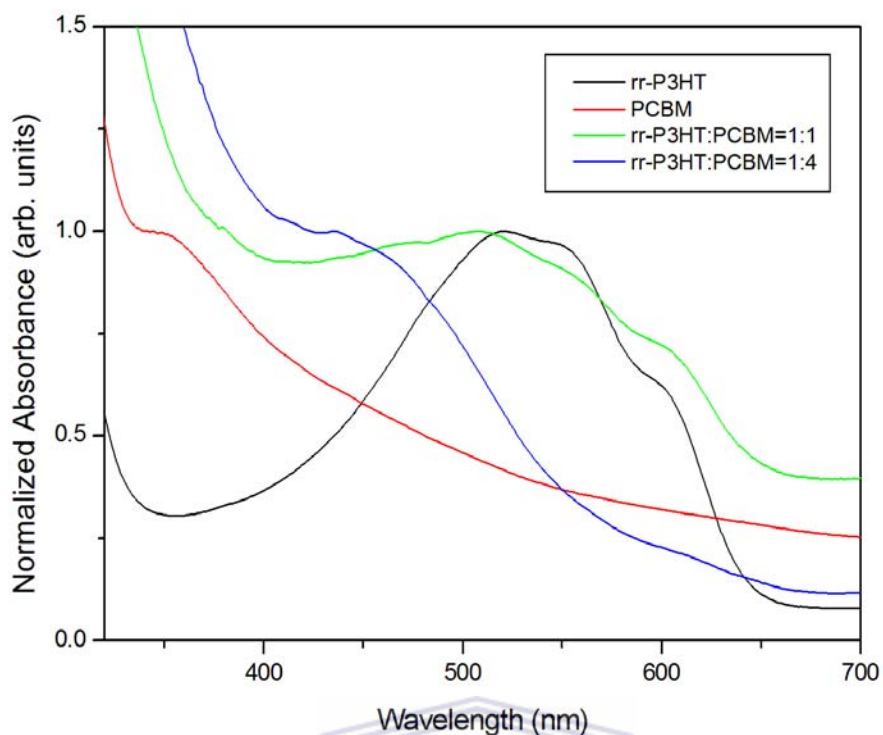
Figure 3.1   Normalised UV-VIS absorption spectra of rr-P3HT, PCBM and
different blends of rr-P3HT:PCBM.

Table 3.1 λ_{max} for rr-P3HT and different blends of rr-P3HT:PCBM.

rr-P3HT:PCBM weight ratio	λ_{max} (nm)	Blue shift relative to rr-P3HT (nm)
rr-P3HT	522	-
rr-P3HT:PCBM = 1:1	507	15
rr-P3HT:PCBM = 1:4	435	87

Various authors reported on the shift in the spectra of rr-P3HT thin film [3.13 – 3.16].
A red shift generally indicates an increase in ordering of the polymer chains. These
changes are attributed to an increasing interchain interaction among the rr-P3HT
chains, due to the ordering of the alkyl side chains within the main thiophene chain;

72

and therefore an increase in the structural ordering. It is also indicative of strong interchain-interlayer interaction among the rr-P3HT chains, which results from an increase in effective conjugated length in the main backbone of the polymer. Therefore, the modification of the absorption spectra of the rr-P3HT:PCBM blended thin films, i.e. the shift to shorter wavelength (blue-shift) when the polymer is blended with increasing PCBM weight ratio, suggests an increase in disorder of the P3HT chains.

Shrotriya et al [3.12] suggested that another possible interaction between rr-P3HT and PCBM might be possible, since rr-P3HT can be oxidized and PCBM can be reduced. The changes in the absorption spectra can therefore also be attributed to the changes in the chemical structure and crystallinity of rr-P3HT, which will be discussed in the next chapter. In particular, any significant non-reversible, non-photoinduced charge transfer between rr-P3HT and PCBM and the degree of rr-P3HT disorder will be verified.

3.3.2 EMISSION PROPERTIES

Photoluminescence (PL) is a process by which a substance absorbs photons and re-radiates it through various mechanisms. Therefore this technique is widely used to investigate the energy levels of materials, thereby providing fundamental information on the electronic properties and impurity levels of these materials.

Figure 3.2 shows the PL emission spectrum of the photo-excited rr-P3HT film. The spectrum was deconvoluted into three emission peaks by a Gaussian fitting procedure

to obtain the electronic states in the photo-excited rr-P3HT film. Three vibronic structures were resolved at 652, 704 and 787 nm. The data of the Gaussian fitting procedure with their calculated energies are presented in Table 3.2. The PL emission peak located at 652 nm (1.90 eV) is assigned to the pure electronic transition from the conduction to the valence band, whereas the peak at 704 nm (1.77 eV) is assigned to the first vibronic band [3.17]. The origin of the emission peak situated around 787 nm (1.58 eV) is unknown. However, emission in the higher wavelength region generally indicates ordering in the rr-P3HT lamella crystallites within the spherical structures, called spherulites [3.18, 3.19].
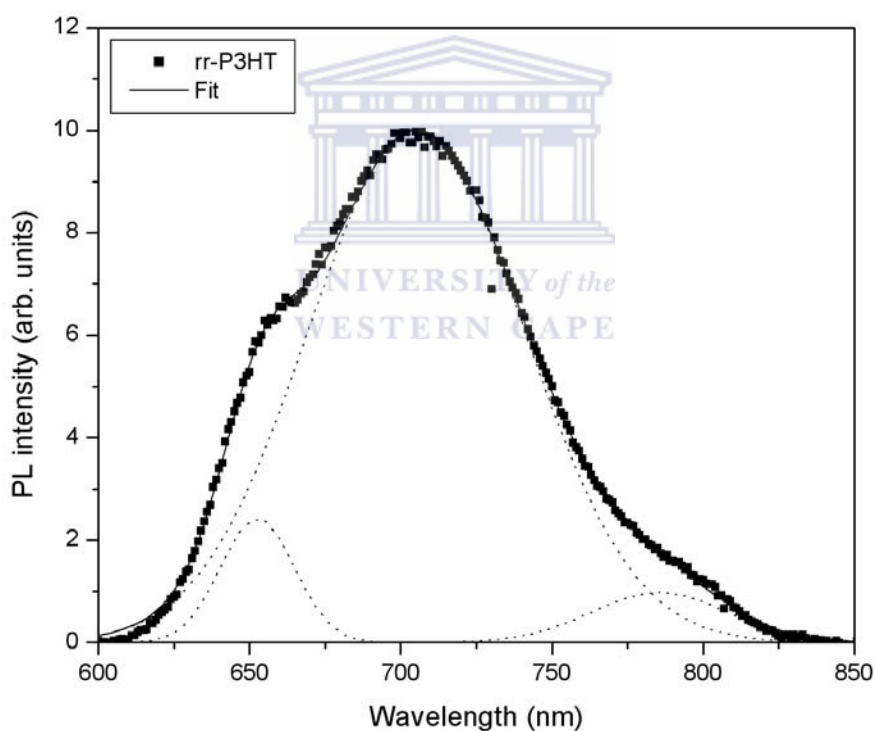

Figure 3.2   PL emission spectrum of the photo-excited rr-P3HT film deposited on a c-Si substrate and its deconvoluted Gaussian peaks.

Table 3.2   PL peaks, wavelength and calculated energies for photo-excited rr-P3HT.

Peak	Wavelength (nm)	Energy (eV)
1	651.98	1.90
2	704.32	1.77
3	787.43	1.58

In addition to the information on the properties of the energy levels that were obtained within rr-P3HT, the PL spectra of rr-P3HT and its blend with PCBM were also measured to ascertain whether there is any interaction between the two materials when photo-excited, as depicted in Figure 3.3. The quenching of PL of an appropriate donor polymer by a suitable acceptor gives an indication of an effective donor-acceptor charge transfer, since dissociation of the created electron-hole pairs (excitons) occur within the ultra short picosecond range compared to the competitive recombination processes like photoluminescence which is in the order of microseconds [3.20].
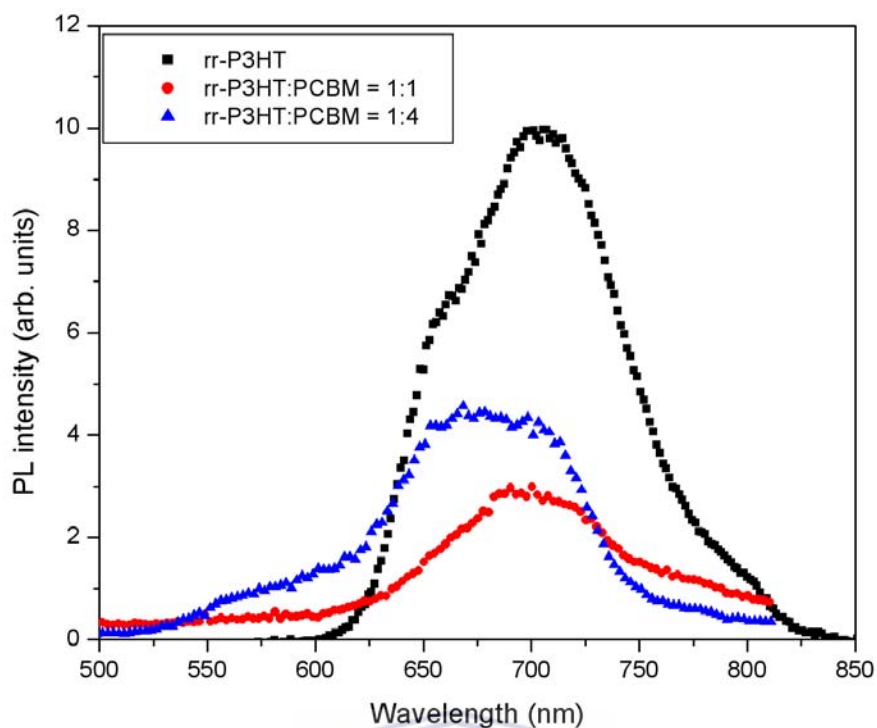
Figure 3.3   PL emission spectra of films of rr-P3HT and different blends of rr-
P3HT:PCBM.
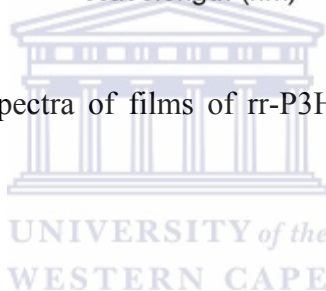
The PL intensity is reduced by a factor of more than 3 for the rr-P3HT:PCBM thin

film mixed with a 1:1 weight ratio of PCBM. This quenching is ascribed to an

effective photo-induced charge transfer process between the rr-P3HT and PCBM.

Contrary to our results, previous literature [3.21, 3.22] show that the PL in P3HT is

completely quenched when mixed with a 1:1 weight ratio of PCBM. The degree of PL

quenching can also be related to the adsorption of oxygen on surface-active sites and

the structural order of the polymer film [3.23]. Therefore, the relative large initial PL

intensity of the rr-P3HT film and the subsequent incomplete quenching with a 1:1

weight ratio of PCBM could be suggestive of surface oxidation defects on the exposed

films. However, more work is necessary to confirm this.

Further loading with PCBM with a weight ratio of 1:4 results in an increase in the PL intensity, indicative of an ineffective charge-transfer process. It is unclear whether the incomplete quenching resulted from reduced exciton mobility on the polymer chains or from pore size simply being too large given the small exciton diffusion length that has been observed in thiophene-based polymers [3.24]. Furthermore, a blue shift to lower wavelength is observed for the blended thin films. This spectral shift has been attributed to an increase in the structural disorder of the rr-P3HT chains [3.23], which is consistent with the UV-VIS results.

We conclude that the change in the PL intensity originates from phase separation and thus from the morphology of the active layer. Improved quenching of the rr-P3HT:PCBM thin film with a 1:1 weight ratio indicates that due to a finer phase separation in the chloroform solution, most of the PCBM is in close enough contact with the polymer, which consequently results in an improved change transfer mechanism between the rr-P3HT and the PCBM. The reduced quenching of the rr-P3HT:PCBM thin film blended to a 1:4 weight ratio is ascribed to the formation of phase separated clusters or agglomerates of PCBM islands within the polymer matrix. Charges become trapped on these PCBM islands and consequently act as recombination sites, thereby resulting in an increased recombination rate as evident by the increased PL intensity.

3.3 CONCLUSION

In this chapter we have probed the opto-electronic properties of rr-P3HT and rr-P3HT:PCBM blended thin films using UV-VIS and PL spectroscopy. The absorption of rr-P3HT in the visible range showed a significant blue shift with an increase in PCBM loading in the blended thin film, attributed to the lowering of the interchain interaction and a non photo-induced charge transfer between rr-P3HT and PCBM in the solid state. The interaction between the rr-P3HT and PCBM not only reduced the order within the polymer chain, which is detrimental for charge transport, but also decreased the potential overlap of the absorption spectra of the blended thin films and the solar emission spectrum. This will subsequently impact negatively on the current density and efficiency of such an OPV device.
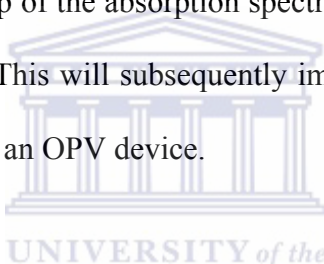
The PL results showed improved quenching when the polymer is blended with PCBM in a 1:1 weight ratio, which indicates superior charge transfer from the polymer donor to the PCBM acceptors, due to a finer phase separation in this blend ratio. The incomplete quenching in this blend could be attributed to surface-active sites, which could easily react with oxygen thereby giving an unwanted PL signal. Further loading with PCBM to a 1:4 ratio results in a reduced quenching and is attributed to the ineffective charge transfer process caused by the formation of phase separated clusters or agglomerates of PCBM islands within the polymer matrix. A blue shift in the PL spectra with increasing PCBM loading was observed and is ascribed to an increase in the structural disorder within the rr-P3HT chains.

REFERENCES

[3.1]   H. Spanggaard, F.C. Krebs, Sol. Energy Mater. Sol. Cells 83 (2004) 125.

[3.2]   Special issue on organic-based photovoltaics, MRS Bull. 30 (1) (2005)

[3.3]   B. Maennig, J. Drechsel, D. Gebeyehu, P. Simon, F. Kozlowski, A. Werner, F. Li, S. Grundmann, S. Sonntag, M. Koch, K. Leo, M. Pfeiffer, H. Hoppe, D. Meissner, N.S. Sariciftci, I. Riedel, V. Dyakonov, J. Parisi, Appl. Phys. A 79 (2004) 1

[3.4]   H. Hoppe, N.S. Sariciftci, J. Mater. Rev. 19 (2004) 1924

[3.5]   C.J. Brabec, Sol. Energy Mater. Sol. Cells 83 (2004) 273

[3.6]   C. Winder, N.S. Sariciftci, J. Mater. Chem. 14 (2004) 1077

[3.7]   C.J. Brabec, S.E. Shaheen, T. Fromherz, F. Padinger, J.C. Hummelen, A. Dhanabalan, R.A.J. Janssen, N.S. Sariciftci, Synth. Met. 121 (2001) 1517.

[3.8]   S.-S. Sun, N.S. Sariciftci, Organic Photvoltaics-Mechanisms, Materials, Devices, CRC Press, Boca Raton, FL, ISBN 0-8247-5963-X (2005)

[3.9]   D. H. Kim, Y. D. Park, Y.S. Jang, H. C. Yang. Y. H. Kim, J.I. Han, D. G. Moon, S. J. Park, T. Y. Chang, C. W. Chang, M. K. Joo, C. Y. Ryu, K.W. Cho, Adv. Func. Mater. 15 (2005) 77

[3.10]   N. Camaioni, G. Ridolfi, G. C. Miceli, G Possamai, M. Maggini, Adv. Mater. 14 (2002) 1735

[3.11]   I. Riedel, V. Dyakonov, Phys. Status Solidi (a) 201 (2004) 1332

[3.12]   V. Shrotriya, J. Ouyang, R.J. Tseng, G. Li, Y. Yang, Chem. Phys. Lett. 411 (2005) 138

[3.13]   T. –A. Chen, X. Wu, R.B. Rieke, J. Am. Chem. Soc. 117 (1995) 233

[3.14]   R.D. Mc Cullough, S. Tristram-Nagle, S.P. Williams, R.D. Lowe, M. Jayaraman, J. Am. Chem. Soc. 115 (1993) 4910

[3.15]   H. Sirringhaus, N. Tessler, R.H. Friend, Science 280 (1998) 1741

[3.16]   H. Sirringhaus, P.J. Brown, R.H. Friend, M.M. Nielsen, K. Bechgaard, B.M.W. Langeveld-Voss, A.J.H. Spiering, R.A.J. Janssen, E.W. Meijer, P. Herwig, D.M. de Leeuw, Nature 401 (1999) 685

[3.17]   M. Sharma, D. Kaushik, R.R. Singh, R.K. Pandey, J. Mater. Sci.: Mater. Electron. 17 (2006) 537

[3.18]   L. Li, C-M. Chan, K.L. Yeung, J.-X. Li, K.-M Ng, Y. Lei, Macromolecules 34 (2001) 316

[3.19]   H. Yang, T. Shin, J.L. Yang, K. Cho, C.Y. Ryu, Z. Bao, Adv. Funct. Mater. 15 (2005) 671

[3.20]   N.S. Sariciftci, L. Smilowitz, A.J. Heeger, F. Wudl, Science 258 (1992) 1474

[3.21]   D.E Motaung, G.F. Malgas, C.J. Arendse, S.E. Mavundla, D. Knoesen, Mater. Chem. Phys. 116 (2009), 279

[3.22]   G.F. Malgas, C.J. Arendse, S.E. Mavundla, F.R. Cummings, J. Mater. Sci. 43 (2008) 5599

[3.23]   K.Y. Jung, S.B. Park, M. Anpo, J. Photochem., Photobibl. A: Chem. 170 (2005) 247

[3.24]   M. Theander, A. Yartsev, D. Zigmantas, V. Sundstrom, W. Mammo, M.R. Anderson, O. Inganasm, Phys. Rev. B 61 (2000) 12957

CHAPTER 4

Structural Properties

4.1 INTRODUCTION

Polymers with low band gaps must be utilised to harvest most of the sun's solar flux in order to improve the efficiency of OPV devices. Regioregular P3HT has an absorption edge of around 650 nm, which translates into a band gap of ~ 1.9 eV. In the previous chapter the blue shift in the absorption and emission spectra of rr-P3HT, when blended with PCBM, have been attributed to the transformation of the chemical and crystalline structure of rr-P3HT. This effect will impact negatively on the current density and hence the efficiency of such an OPV device as a result of a mismatch with the sun emission spectrum. In addition, the overall power conversion not only depends on how well the rr-P3HT:PCBM blended thin film optical absorption band overlaps with solar emission, but also depends on factors intrinsic to the OPV device as well.

In fact, there are several factors that influence the efficiency of OPVs. This includes the structure of the polymer, the morphology of the film, the interfaces between the layers, the choice of electron acceptor and the ratio between this and the polymer. Much effort is put in understanding the device physics and optimising the efficiency

of these cells. A prerequisite for optimising the efficiency is the fundamental understanding of the relation between structural properties and the opto-electronic properties.

In this chapter we report on the structural changes that occur in the rr-P3HT film when blended with different ratios of PCBM and correlate this to the optical properties discussed in Chapter 3. Fourier transform infrared spectroscopy and Raman spectroscopy were used to probe the chemical structural changes, while X-ray diffraction and high-resolution transmission electron microscopy were used to investigate the crystalline structure.

4.2 EXPERIMENTAL

4.2.1 SAMPLE PREPARATION

It should be noted that the same chemicals were used to investigate the structural changes than those used to evaluate the optical properties in the previous chapter. The sample preparation procedure is identical to that mentioned in Section 3.2.1.

4.2.2 CHARACTERISATION

Fourier transform infrared (FTIR) absorption spectra were collected in transmission geometry from $400 - 400$ cm^{-1} with a spectral resolution of 1 cm^{-1}, using a Perkin-Elmer Spectrum 100 FTIR spectrophotometer. The structural properties were also investigated using a Jobin-Yvon HR800 micro-Raman spectrometer in backscattering

geometry at room temperature. The Raman spectra were collected in the region 100 – 3000 cm^{-1} with a spectral resolution of 0.4 cm^{-1}, using a 514.5 nm Ar^{+} excitation laser. X-ray diffraction (XRD) spectra were collected in reflection geometry at 2θ-values ranging from 3 – 40°, with a step size of 0.02°, using a PANalytical® X-ray powder diffractometer operating at 45 kV and 40 mA. Monochromatic Copper (Cu) Kα$_1$ radiation with a wavelength of 0.154 nm was used as the X-ray source. An FEI Tecnai F20 field emission high-resolution electron microscope (HR-TEM), operated at 120 kV was employed to examine the internal structure and crystallinity of the different samples. Specimens for HR-TEM analysis were prepared by transferring a small drop of each solution of rr-P3HT and its blends with PCBM on a holey-carbon copper grid and dried at ambient conditions.

4.3 RESULTS AND DISCUSSION

4.3.1 CHEMICAL STRUCTURE

Fourier transform infrared spectroscopy (FTIR) has been identified as the technique of choice to investigate the transformation in the chemical structure of rr-P3HT when blended with PCBM as a result of its simplicity, short time and non-destructive nature. The raw (untreated) FTIR absorbance spectra of the thin films of rr-P3HT, PCBM and different blends of rr-P3HT:PCBM are depicted in Figure 4.1.

The FTIR absorption bands for rr-P3HT are summarised in Table 4.1. The peaks centred around 2856, 2925 and 2955 cm^{-1} are assigned to the CH$_2$ out-of-phase stretching, CH$_2$ in-phase stretching and the CH$_3$ asymmetric stretching vibrations,

respectively. The peaks centred at 1507 and 1457 cm^{-1} represent the C=C asymmetric stretching and the C−C symmetric stretching modes, respectively. A new, unidentified band emerges for the blends around 1112 cm^{-1}, which is not due to any vibrations from the PCBM. It should be noted that this band has not been reported in literature for rr-P3HT and PCBM. Lastly, the absorption bands at 819 and 721 cm^{-1} are assigned to the C−H out-of-plane and CH$_3$ rocking vibrations, respectively.
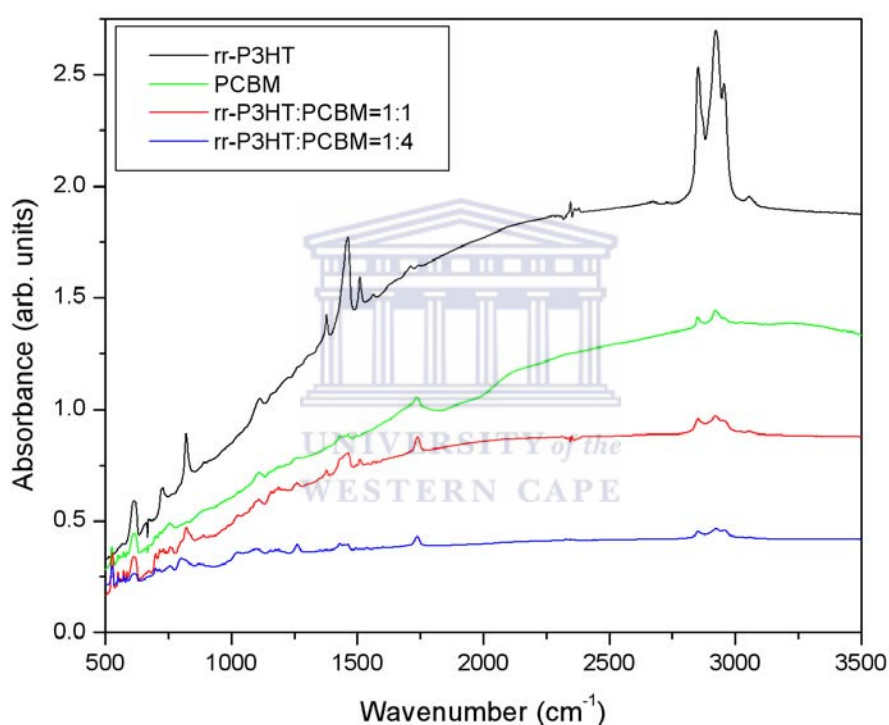

Figure 4.1   FTIR absorbance spectra of rr-P3HT, PCBM and different blends of rr-P3HT:PCBM.

The average conjugation length of a polymer is defined as the length over which the backbone planarity is maintained without interruption and which defines the chromophore. In particular, the effective conjugation length along the polymer backbone of rr-P3HT can be interpreted as the length of a completely undisturbed

alternating single bond / double bond segment, being planar and allowing maximum overlap of the π-electrons. Therefore, the ratio (R) of the intensities of the asymmetric C=C stretching peak (I_{1509}) to the symmetric C–C stretching peak (I_{1456}) can be used as a measure for the effective conjugation length [4.1, 4.2]. To investigate the evolution of the R-ratio, a third order polynomial background subtraction was performed on the raw absorbance spectra. Subsequently, the spectra were normalized to enhance any distinguishable features between rr-P3HT and its blends with PCBM, shown in Figure 4.2.

Table 4.1   FTIR absorption bands and assignments of rr-P3HT.

rr-P3HT wavenumber (cm^{-1})	Assignment
721	Methyl rock mode
819	C–H out of plane deformation mode
1112	-
1377	Methyl deformation mode
1507	Ant-symmetric C=C stretching mode
1457	Symmetric C–C stretching mode
2856, 2925, 2955	Aliphatic C–H stretching mode

The calculated R-value for rr-P3HT amounts to 0.38; and remains constant after blending with an equal weight percent of PCBM, suggesting that the effective conjugation length of the backbone; and therefore the structural order, of rr-P3HT is maintained. After quadrupling the PCBM weight ratio, a notable reduction in the intensity of the C=C vibration-peak is observed, resulting in a 73 % reduction in the

R-value to 0.1. This implies that the effective conjugation length; and therefore the structural order, of rr-P3HT is reduced due to blending with excessive amounts of PCBM.
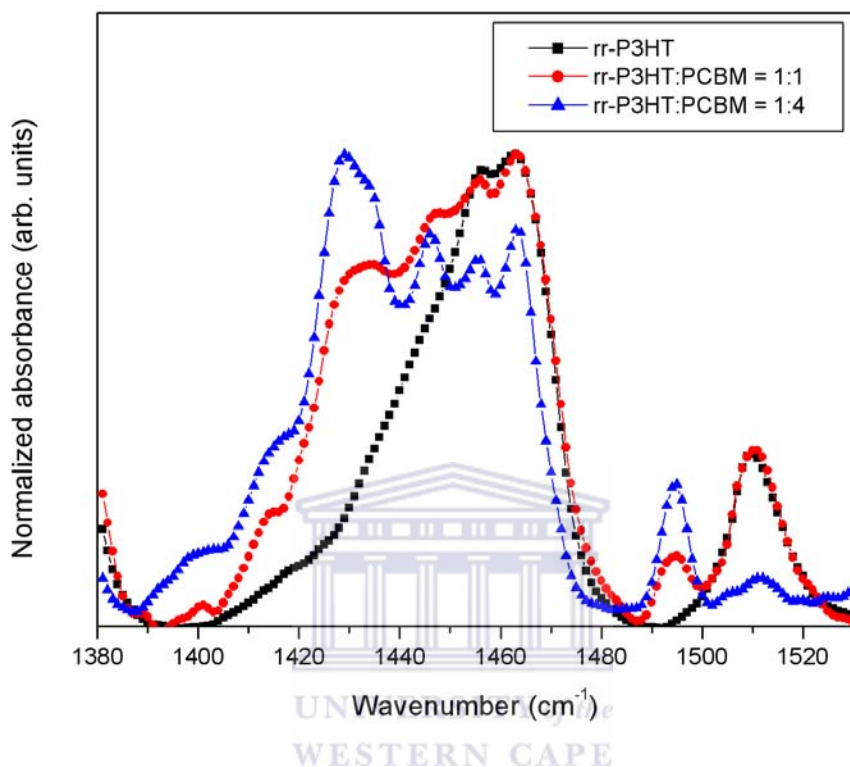

Figure 4.2   FTIR absorbance spectra of the symmetric C=C and C−C vibrations for rr-P3HT and its blends with PCBM.

Therefore, we conclude that excessive blending of rr-P3HT with PCBM has a severe negative impact on the structural quality of rr-P3HT, which can compromise the favourable conditions for an effective charge transfer process created by blending rr-P3HT with an equal PCBM weight ratio. This observation confirms that the blue shift in the UV-VIS absorption and PL emission spectra, discussed in Section 3.3, is attributed to the breakdown of the structural integrity of rr-P3HT when blended with excessive amounts of PCBM.

The vibrations of some compounds are sensitive to changes of the charge on the compounds. In particular, Ouyang et. al. [4.3, 4.5] has illustrated that the peak positions of the C=C and C−S stretching vibrations of rr-P3HT may shift when the amount of charge on the compound is altered. Therefore, the analysis of these absorption peaks can be used to gain qualitative insight into the charge transfer mechanism in rr-P3HT:PCBM blends. However, it is difficult to explain the charge transfer mechanism between rr-P3HT and PCBM from the C=C vibration, since both rr-P3HT and PCBM contain this vibration, which would not allow changes from either compounds to be distinguishable. Furthermore, the C−S stretching vibration of rr-P3HT is not easily observed in its FTIR spectrum [4.3], which is also manifested in Figure 4.1.
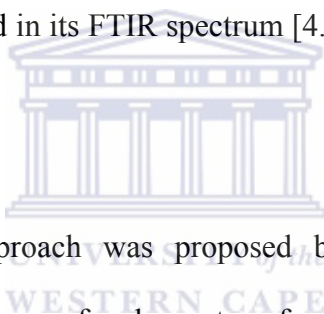
Recently, an alternative approach was proposed by Shrotriya et al [4.5], by demonstrating that the occurrence of a charge transfer process is evidenced by a shift in the position of the absorption band assigned to the C−H deformation vibration associated with the thiophene ring in rr-P3HT. Therefore, the shift in the position of the 819 cm^{-1}-peak can be used to study the charge transfer process in rr-P3HT and PCBM. To investigate the evolution of this peak, the above-mentioned analysis procedures were performed, and the results thereof are depicted in Figure 4.3.

The superior purity and chemical structure of rr-P3HT are illustrated by the symmetric shape of the peak at ~ 819 cm^{-1}. Two new bands at ~ 801 and 835 cm^{-1} appear as shoulders for the 1:1-blend and evolve further after the increasing the PCBM weight ratio. In comparison with the FTIR spectrum of PCBM in Figure 4.1, it

is apparent that these bands do not originate from PCBM. The emergence of the band at 834 cm^{-1} is attributed to the charge transfer that occurs between the sulphur atom in P3HT and the PCBM molecule [4.5]. A specific amount of charge is transferred from the sulphur atoms to the conjugated chains in the PCBM molecules, resulting in a slight positive charge present on the sulphur atoms. To quantify the charge transfer mechanism, the spectra were deconvoluted into three Gaussian curves and the results of this fitting procedure are summarised in Table 4.2. The deconvoluted spectra for the 1:1 and 1:4 blends are shown in Figures 4.4 (a) and (b), respectively.
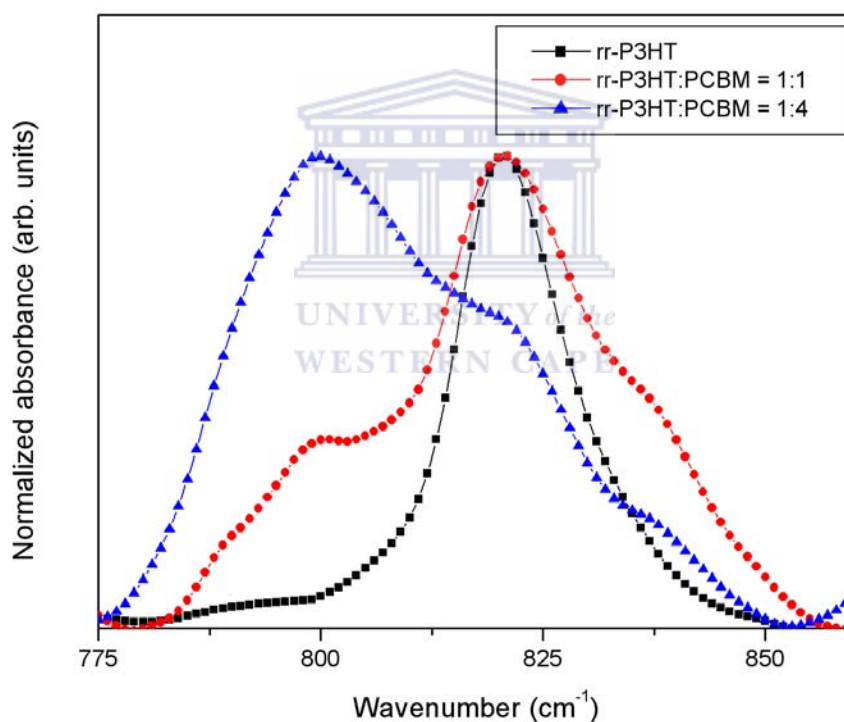

**Figure 4.3**   FTIR absorbance spectra of the C−H deformation vibration for rr-P3HT and its blends with PCBM.
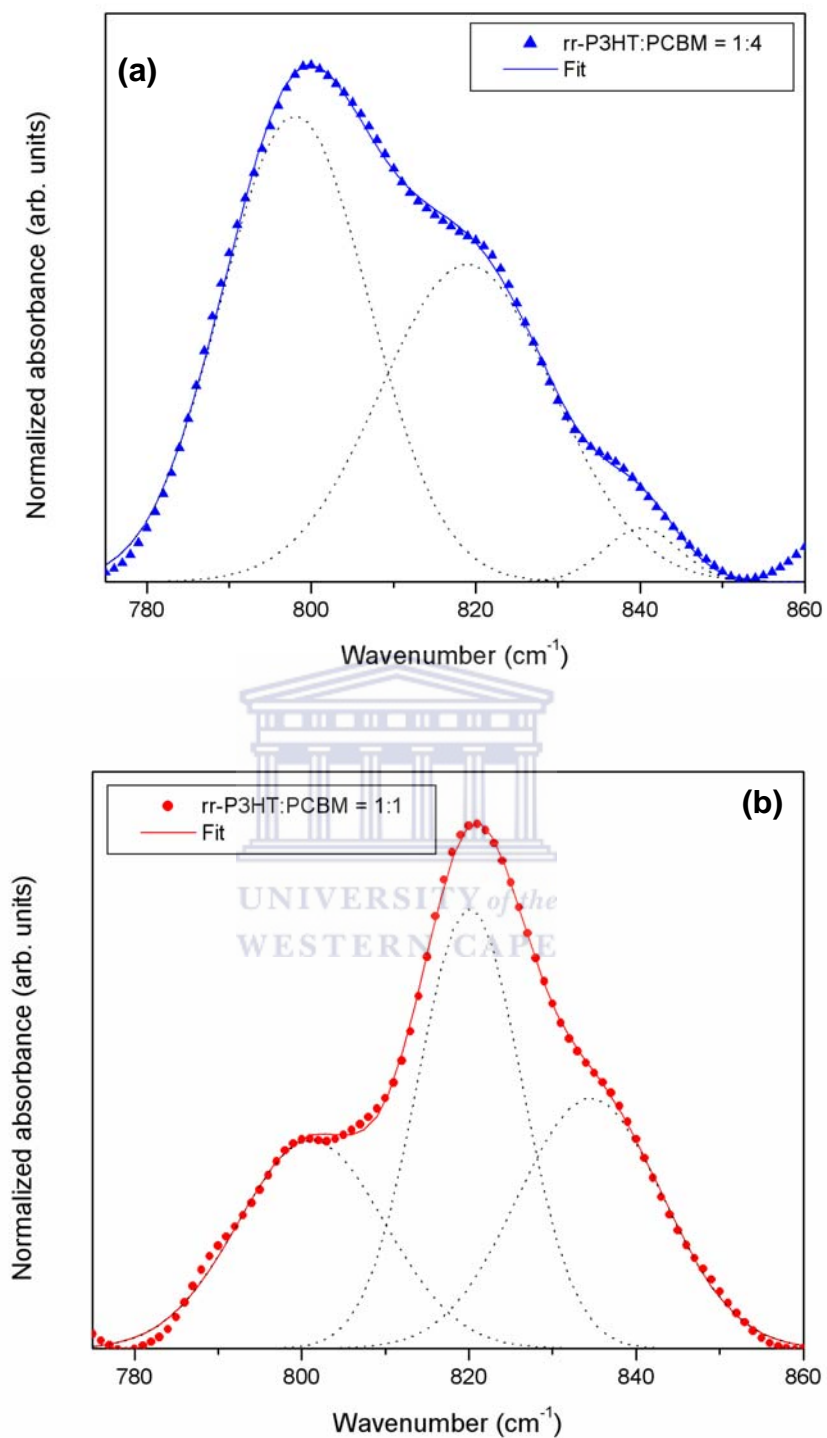
Figure 4.4   The deconvoluted FTIR absorbance spectra of the C−H deformation

vibration for (a) 1:1 and (b) 1:4 blends.

Table 4.2   Summary of results of the fitting procedure of the FTIR absorbance deconvoluted spectra for 1:1 and 1:4 blends.

Peak	Position (cm^{-1})	FWHM (cm^{-1})	Intensity	Area (cm^{-1})
rr-P3HT:PCBM = 1:1				
1	801.15	17.473	0.39857	8.7283
2	820.11	12.457	0.84064	13.124
3	834.54	17.360	0.47850	10.411
rr-P3HT:PCBM = 1:4				
1	798.05	17.894	0.90579	20.314
2	818.99	20.826	0.61502	16.053
3	840.02	9.6179	0.10294	1.2409

A broadening in the peak centred around 819 cm^{-1} is observed with the addition and the further increase in the weight ratio of PCBM, as seen by the increase in the full-width-at-half-maximum (FWHM) in Table 4.2. The broadening is attributed to an increase in the variation of the C–H deformation vibrational energy, caused by an increase in the structural disorder. This illustrates that an increase in the weight ratio of PCBM results in an increased structural disorder of rr-P3HT, consistent with the observed reduction in the R-values reported above.

The integrated area of the band at 834 cm^{-1}, associated with the charge-transfer mechanism, can be used as a measure for the charge transfer process. Therefore, for quantitative analysis of the charge transfer process, we define the charge transfer

indicator (f_{ct}) as the ratio of the integrated area of the 834 cm^{-1}-peak to the total

integrated area of the 819 and 834cm^{-1}-peaks; and is given by:

$$f_{ct} = \frac{A_{834}}{A_{819} + A_{834}} \tag{4.1}$$

where A_{819} and A_{834} is the integrated area of the 819 and 834cm^{-1}-peaks, respectively.

Using equation (4.1), a charge transfer indicator of 50 % is calculated for the 1:1

blend of rr-P3HT:PCBM and decrease by at least one order of magnitude to 5% for

the 1:4 blend. This confirms that the reduction in the structural order in rr-P3HT,

induced by blending with excessive amounts of PCBM, is accompanied by a

reduction in its charge transfer mechanism. This result therefore supports the notion of

a significant non-reversible non-photoinduced charge transfer between rr-P3HT and

PCBM, as proposed by Shrotriya et al [4.5].

Due to its sensitivity to minute changes in the chemical structure of rr-P3HT, Raman

spectroscopy was employed as a complementary technique to probe specific changes

in the chemical structure of rr-P3HT and its blends with PCBM. Figure 4.5 shows the

Raman spectra of rr-P3HT, PCBM and different blends of rr-P3HT:PCBM. The

spectrum features all the vibrational frequencies expected from the conjugated

polymer.

The band at 1518 cm^{-1} can be assigned to C_α–C_β antisymmetric vibrations in the

aromatic thiophene ring [4.6, 4.7]. The band in the vicinity of 1445 – 1455 cm^{-1} is due

to symmetric $C_\alpha = C_\beta$ stretching deformation. The band at 1378 cm^{-1} is due to C_β–C_β stretching deformation in the aromatic thiophene ring. Two bands at lower wavenumbers (1210 and 1186 cm^{-1}) are ascribed to C_α–C_α symmetric stretching and C_β–H bending, respectively. The peak at 726 cm^{-1} is due to C–S–C ring deformation. Finally, the peak at 520 cm^{-1} is ascribed to the transverse-optical vibration of the crystalline silicon substrate.
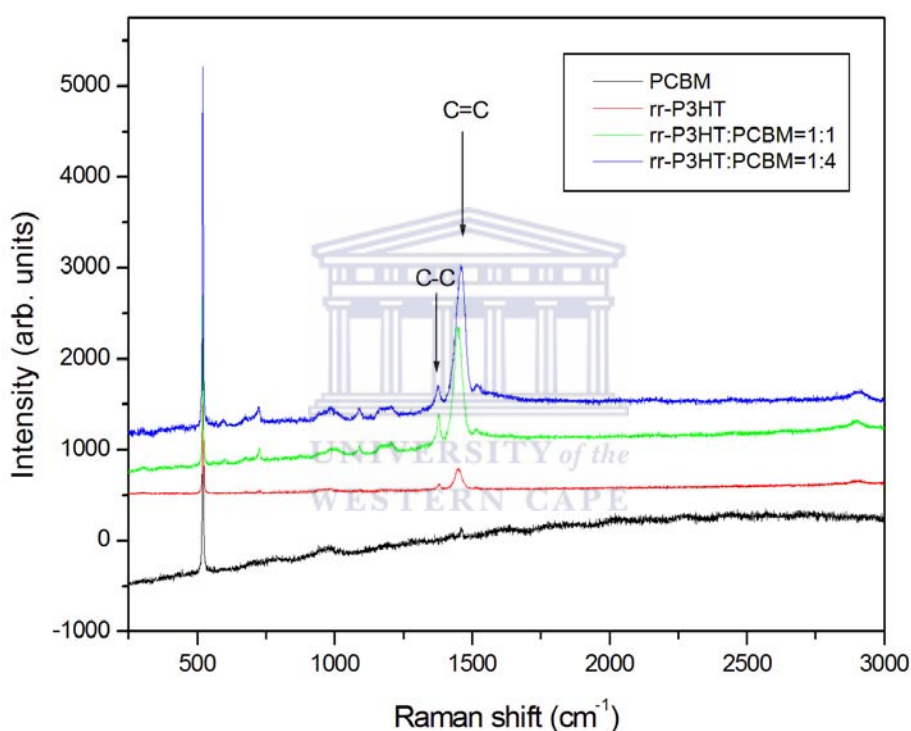

Figure 4.5   Raman spectra of rr-P3HT, PCBM and different blends of
                   rr-P3HT:PCBM.

To gain additional insight into the Raman spectra, the region around 1450 cm^{-1} was further probed (see Figure 4.6). The peak position corresponding to the symmetric $C_\alpha = C_\beta$ stretching deformation, is shifted to a higher wavenumber for the rr-P3HT:PCBM blend corresponding to 1:4 weight ratio. Blends of rr-P3HT:PCBM

corresponding to weight ratios of 1:1 does not show any appreciable shift in wavenumber. Heller et. al. [4.8] suggested an increase in wavenumber generally indicates a decrease in order/crystallinity in the conjugated polymer which corresponds to a decrease in the effective conjugated length of the polymer backbone.

The results obtained from the Raman spectra corroborate with that of FTIR spectroscopy, by suggesting that an increase in the rr-P3HT:PCBM blend ratio reduces the effective conjugated polymer length of the polymer backbone and hence the order within the polymer. As a result, the polymer film prepared with rr-P3HT:PCBM weight ratio of 1:1 has favourable molecular morphologies for transport of charge carriers and hence improved cell efficiencies.
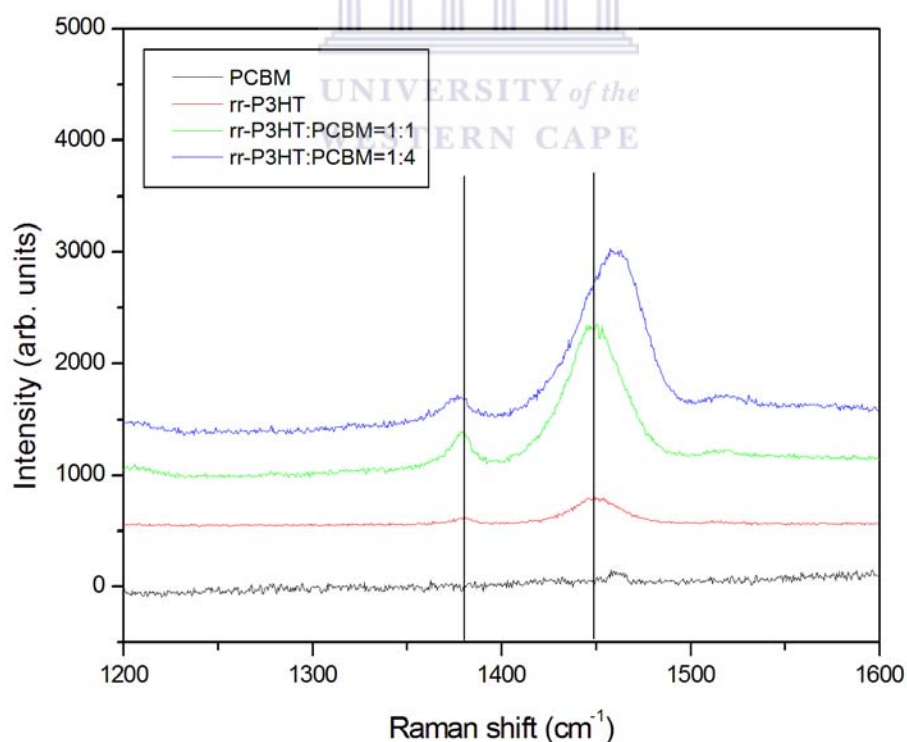

Figure 4.6   Raman spectra of rr-P3HT, PCBM and its blends of rr-P3HT:PCBM in the region of 1450 cm^{-1}.

4.3.2 CRYSTALLINE STRUCTURE

X-ray diffraction was employed to acquire morphological information (crystallinity and chain orientation) of the rr-P3HT film and its blends with PCBM. Figure 4.7 depicts the XRD pattern of rr-P3HT, in powder form, which shows three peaks at 2θ = 5.33°, 10.66° and 16.07 ° which corresponds to the (100), (200), (300) reflections. These well defined diffraction peaks correspond to an ordered, self-organised lamellae structure with an interlayer spacing, which is formed by parallel stacks of polymer main stains that are separated by regions that are filled with hexyl side chains [4.9-4.14].

The corresponding d-spacing for these different reflections can be calculated using Bragg's law. Using λ = 0.154 nm, the wavelength of the incident beam, 2θ the angle between the incident and the scattered X-ray wave vector, and n the interference order, we obtain d-spacing values of 16.56 nm, 8.29 nm and 5.51 nm for the (100), (200) and (300) reflections, respectively.

The polymer backbone orientation within these crystallites appears to be parallel to the substrate, which can be attributed to twice the hexyl side chain length (see figure 4.8). These side-chains are therefore orientated perpendicular to the substrate (along the a-axis). No other orientations (as indicated by the arrow where they should be expected) of the rr-P3HT crystals could be observed and thus there appear to be a preferential orientation of polymer molecules on the substrate. This observation of preferential orientation could be easily verified with Transmission Electron Microscopy (TEM), which measures d-spacing perpendicular to the surface. The d-

spacing of the c-axis, and not the a-axis, should therefore be revealed using this technique.
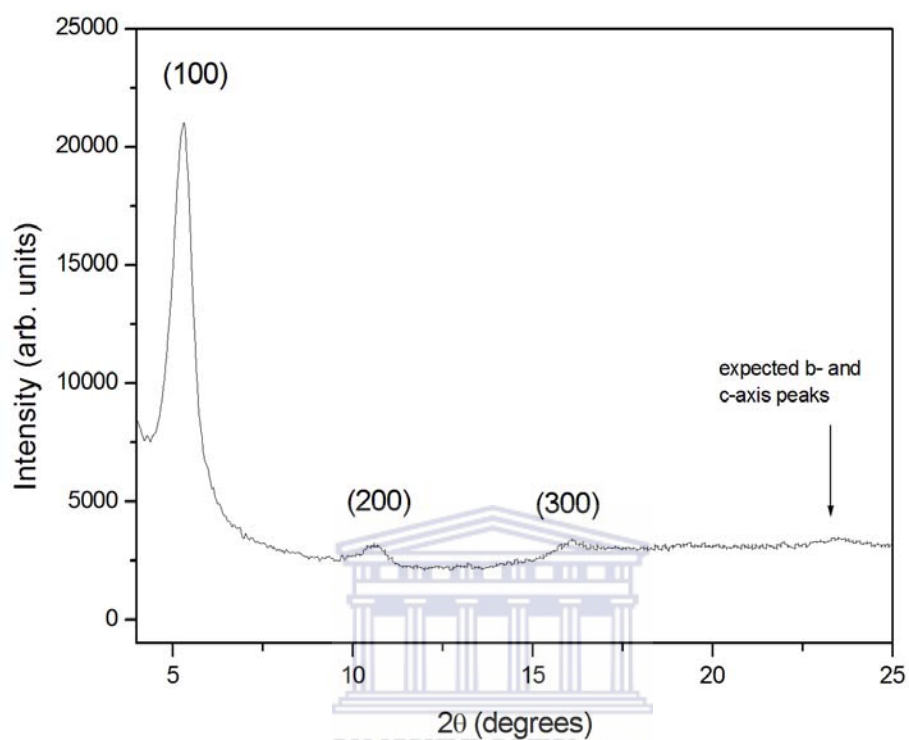

**Figure 4.7**   XRD pattern of rr-P3HT in powder form.
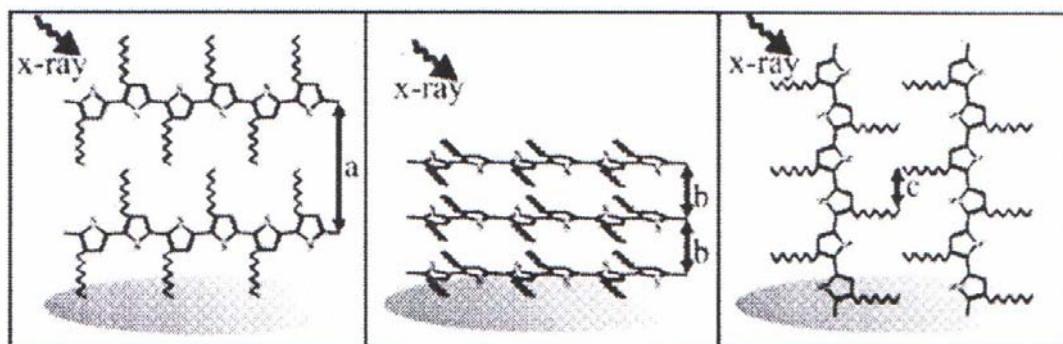
Figure 4.8   Possible crystalline orientations of rr-P3HT-crystallites with respect to the substrate.

The XRD patterns of the thin films of rr-P3HT, PCBM and different blends of rr-P3HT:PCBM that are spin coated on a Si substrate are depicted in Figure 4.9.
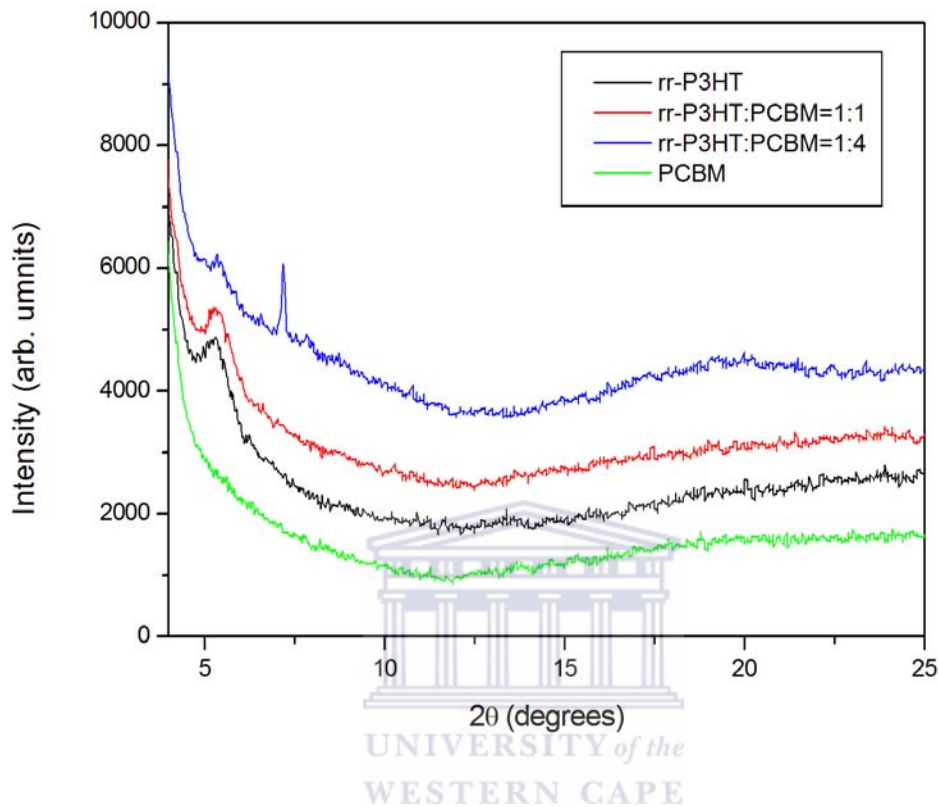

Figure 4.9   XRD patterns of rr-P3HT, PCBM and different blends of rr-P3HT:PCBM that are spin coated on a Si substrate.

The pattern of rr-P3HT and its blends shows one distinct peak at around $2\theta = 5.33°$, which is due to the (100) reflection. The absence of the (200) and (300) reflections is indicative of the thickness of the film which in this case was spin coated. In addition, no other diffraction peaks corresponding to the P3HT crystallites with other orientations such as polymer backbone perpendicular to substrate (or side chains parallel to substrate) were observed. A diffraction peak at around $2\theta = 7.10°$, for PCBM evolved due to excessive loading of PCBM with the polymer for P3HT:PCBM weight ratio of 1:4. However, it must be noted that Chiu et. al. [4.15] showed that

when rr-P3HT is blended with PCBM, the crystallite size reduces with an increase in annealing temperature. They also showed that the particles of PCBM become larger and subsequently lead to better pathways for electron transport.

Kline et al. [4.16] reported that rr-P3HT films with higher molecular weight produce a broader XRD peak (increase in FWHM), suggesting a more disordered film with smaller crystalline domains. An increase in crystal size (reduction in FWHM) indicates an increase in the ordering of the alkyl chains within the main thiophene chain and therefore an increase in the structural ordering. The mean crystal sizes of the rr-P3HT crystallites at (100) reflection L_{100} can be obtained using Scherrer's relation [4.17, 4.18]:
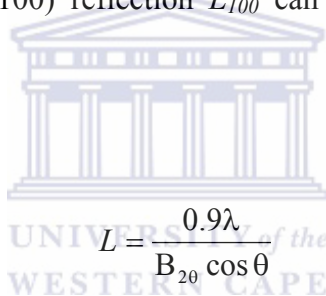
$$L = \frac{0.9\lambda}{B_{2\theta}\cos\theta} \qquad (4.2)$$

where λ is the wavelength of the x-rays, $B_{2\theta}$ the full-width-at-half-maximum (FWHM) and θ the diffraction angle. Therefore, employing Scherrer equation, we obtain the crystal size of rr-P3HT and its blends with PCBM, as shown in Table 4.3.

The crystal size decreases with an increase in PCBM loading (from 1:1 to 1:4), suggesting a more disordered film with smaller crystalline domains [4.16], which is consistent with the UV-VIS, PL, FTIR and Raman spectroscopy results. However, one would expect a maximum mean crystal size for the unblended polymer, but the results show the contrary. This suggests that the crystalline regions of rr-P3HT are not uniformly distributed across the substrate surface. This observation was verified by

comparing the FWHM measured at two different spots on the rr-P3HT sample (see Table 4.3), which confirms this hypothesis.

Table 4.3   Crystal sizes of rr-P3HT and its blends with PCBM.

rr-P3HT:PCBM weight ratio	Reflection	d-spacing (nm)	FWHM (degrees)	Crystal size (nm)
rr-P3HT (spot 1)	(100)	1.66	0.51	19.45
rr-P3HT (spot 2)	(100)	1.66	0.41	0.34
rr-P3HT:PCBM=1:1	(100)	1.70	0.26	30.66
rr-P3HT:PCBM=1:4	(100)	1.65	0.31	25.98

High-resolution transmission microscopy (HR-TEM) was further employed to examine the internal structure and crystallinity of rr-P3HT and its blends with PCBM. The HR-TEM micrograph presented in Figure 4.10 illustrates that the rr-P3HT is crystalline. The micrograph shows a homogeneous layer without any obvious phase separation. The inset in Figure 3.10 corresponds to the fast Fourier transform (FFT) of the selected square area. The FFT shows a low degree of crystallinity for rr-P3HT, which confirms that the material is composed crystalline domains embedded in an amorphous matrix [4.19, 4.20]. The d-spacing, calculated from the FFT, is estimated to be approximately 0.38 nm, which corresponds to the (001) plane.

This is not a contradiction from the earlier results obtained from XRD, since XRD measures in reflection geometry and reveals the d-spacing normal to the surface, whereas HR-TEM measures in transmission geometry and gives the d-spacing perpendicular to the surface. No other orientations of rr-P3HT crystals could be

observed and thus it appears that the rr-P3HT molecules align itself in a specific direction on the substrate. This preferential orientation was indeed observed in the XRD results.
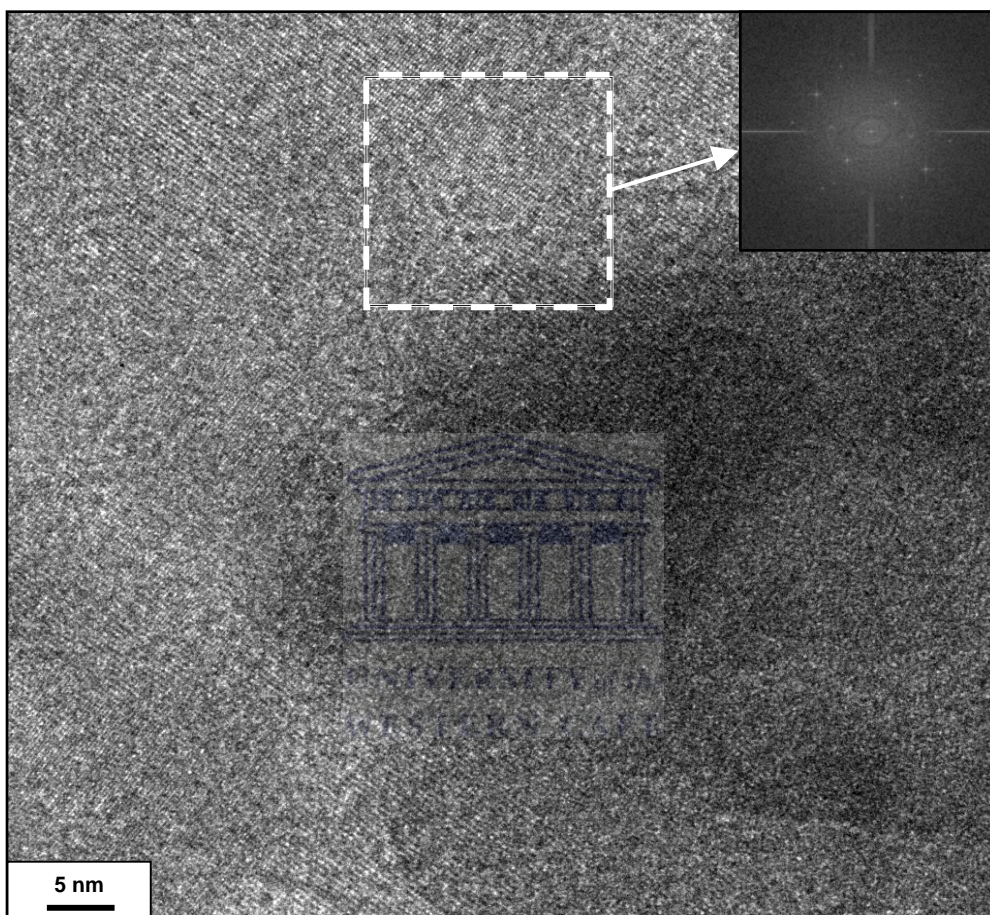

Figure 4.10   HR-TEM micrograph of rr-P3HT. The inset is the FFT of the selected square area.

Figure 4.11 depicts the HR-TEM micrograph of rr-P3HT blended with PCBM with a weight ratio of 1:1. The micrograph shows a similar morphology as Figure 4.10, with the exception that the FFT of the selected square area shows a lower degree of crystallinity of the rr-P3HT film when blended with PCBM. This suggests that the crystallinity of the blended material has decreased.
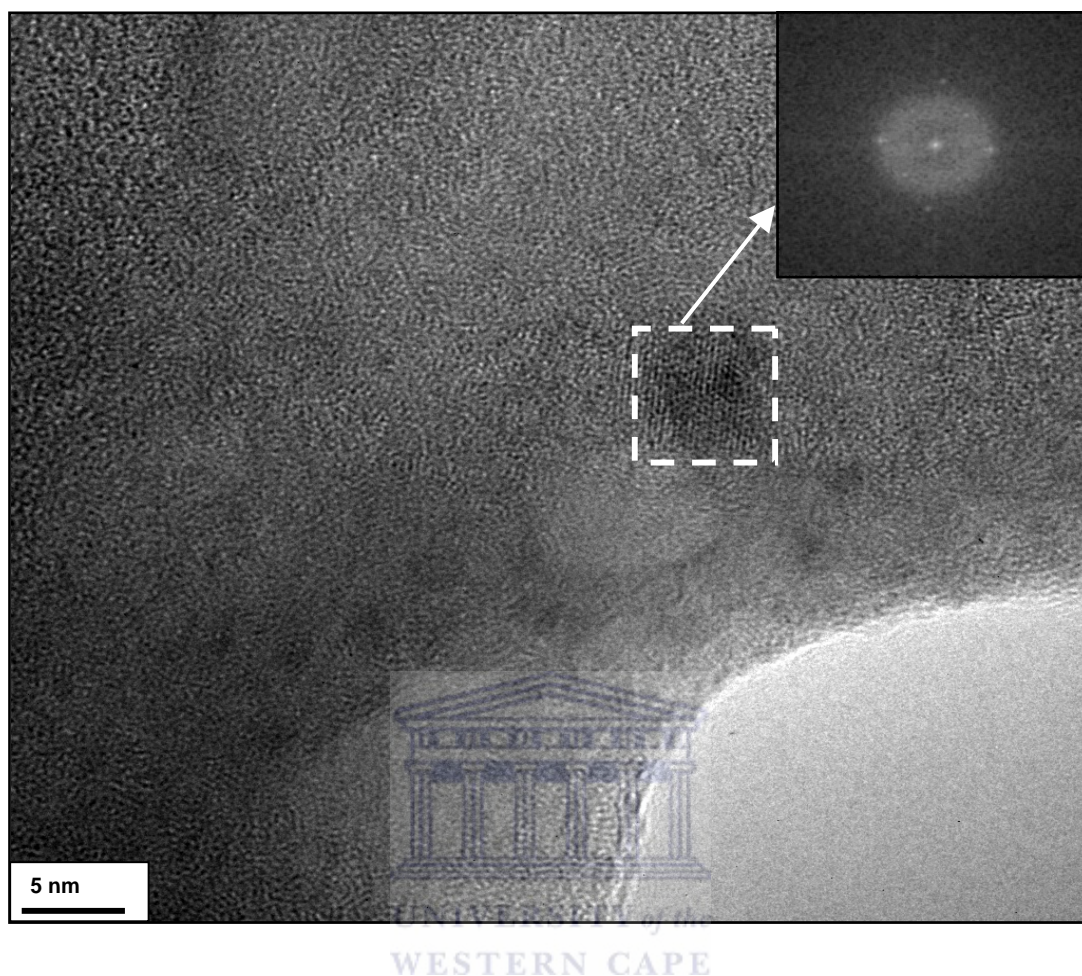
Figure 4.11   HR-TEM micrograph of the rr-P3HT:PCBM =1:1 blend. The inset is
the FFT of the selected square area.

Figure 4.12 depicts the HR-TEM micrograph of rr-P3HT blended with PCBM with a
weight ratio of 1:4. The micrograph shows that the material is amorphous, confirmed
by the FFT results that show no bright spots. Therefore, HR-TEM and XRD results
confirm that loading with excessive amounts of PCBM induces a severe reduction in
the crystallinity and structural integrity of rr-P3HT, consistent with the optical
absorption, emission and spectroscopic observations.

100
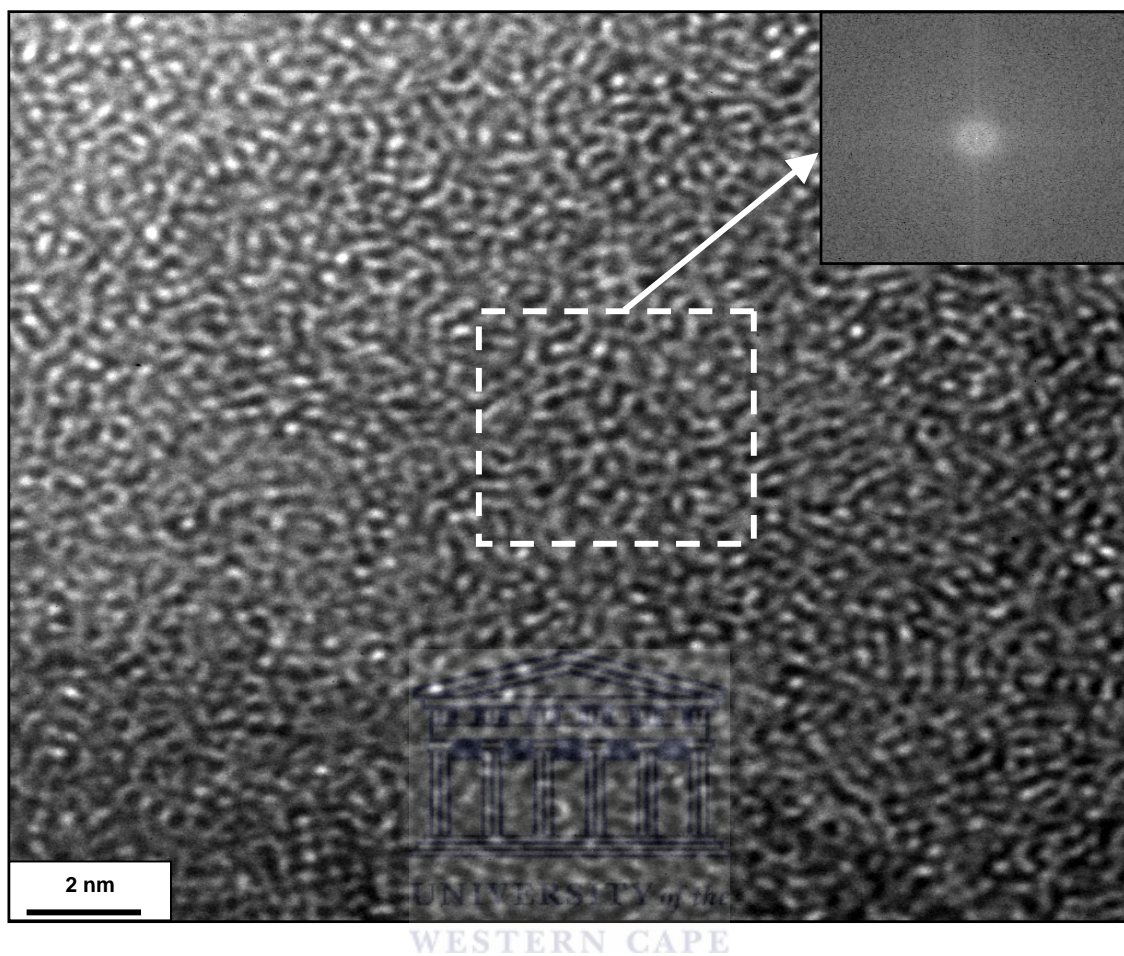
Figure 4.12 HR-TEM micrograph of the rr-P3HT:PCBM =1:4 blend. The inset is the FFT of the selected square area.

4.4 CONCLUSION

In this chapter we investigated the structural and crystalline properties of rr-P3HT films and rr-P3HT:PCBM blended films using FTIR spectroscopy, Raman spectroscopy, XRD and HR-TEM. The changes in the structural and crystalline properties were correlated with changes in the optical properties.

FTIR showed a 73% reduction in R-value (defined as the ratio of the intensities of the asymmetric C=C stretching peak (I_{1509}) to the symmetric C–C stretching peak (I_{1456})) for the 1:4 blend compared to rr-P3HT and 1:1 blend, suggesting that the effective conjugated length and hence the structural order of rr-P3HT is severely compromised due to the blending of excessive amounts with PCBM. In addition, quantitative analysis of the peak at 834 cm^{-1} confirms the reduction in structural disorder in rr-P3HT, induced by blending it with excessive amounts of PCBM, which is accompanied by the reduction in the charge transfer process. These results were further corroborated with Raman spectroscopy, which for the 1:4 blend showed a shift to higher wavenumbers for the C=C stretching deformation peak centered around 1450 cm^{-1}, indicative of an increased disordering in the conjugated polymer.

XRD and HR-TEM demonstrated the crystalline behaviour of rr-P3HT and the 1:1 blend. However, the crystal sizes decreased with an increase in PCBM weight ratio, suggesting a more disordered film with smaller crystalline domains, which corroborates the interpretation of the spectroscopic and optical measurements. Finally,

the d-spacing obtained from XRD and HR-REM indicated a preferred orientation of rr-P3HT on the sample surface.

In summary, rr-P3HT:PCBM blend for the 1:1 ratio showed a higher degree of crystallinity, structural order and a superior charge transfer capability compared to the 1:4 ratio. Therefore, we conclude that blending rr-P3HT with an equal weight of PCBM would result in an optimum configuration for improved performance in organic photovoltaic devices.

UNIVERSITY *of the*
WESTERN CAPE

REFERENCES

[4.1]   Y. Furukawa, M. Akimoto, I. Harada, Synth. Met. 18 (1987) 151

[4.2]   M. Trznadel, A. Pron, M. Zagorska, R. Chrzaszcz, J. Pielichowski, Macromolecules 31 (1998) 5051

[4.3]   J. Ouyang, K. Yakushi, T. Kinoshita, N. Nanbu, M. Aoyagi, Y. Misaki, K. Tanaka, Spectrochim. Acta Part A 58 (2002) 1643

[4.4]   J. Ouyang, K. Yakushi, Y. Misaki, K. Tanaka, Phys. Rev. B 63 (2001) 054301

[4.5]   V. Shrotriya, J. Ouyang. R.J. Tseng, G. Li, Y, Yang, Chem. Phys Lett. 411 (2005) 138

[4.6]   G. Louarn, J.Y. Mevellec, J.P. Buisson, S Lefrant, Synth. Met. 1992, 55-57, 587

[4.7]   Y. Furukawa, M. Akimoto, I Harada, Synth. Met. 1987, 18, 151.

[4.8]   C. Heller, G. Leising, G. Godon, S. Lefrant, W. Fischer, F. Stelzer, Phys. Rev. B 51 (1995) 8107

[4.9]   T. A. Chen, X. Wu, D. Rieke, Amer. Chem. Soc. 117 (1995) 233

[4.10]   W. R. Salaneck, O. Inganas, B. Themas, J. O. Nilsson, B. Siogren, J.E. Osterholm, J.L. Bredas, S. Svensson, J. Chem. Phys. 89 (1988) 4613

[4.11]   P. Vanlaeke, G. Vanhoyland, T. Aernouts, D. Cheyns, C. Deibel, J. Manca, P. Heremans, J. Poortmans, Thin Solid Films 511-512 (2006) 358

[4.12]   P. Vanlaeke, A. Swinnen, I. Haeldermans,G. Vanhoyland, T. Aernouts, D. Cheyns, C. Deibel, J. D'Haen, P. Heremans, J. Poortmans, J. V. Manca, Sol. Energy Mater. & Sol. Cells 90 (2006) 2150

[4.13] T. Erb, U. Zhokhavets, G. Gobsch, S. Raleva, B. Stühn, P. Schilinsky, C. Waldauf, C. J. Brabec, Adv. Funct Mater. 15 (2005) 1193

[4.14] U. Zhokhavets, T Erb, H Hoppe, G. Gobsch, N. S. Sariciftci, Thin Solid Films 496 (2006) 679

[4.15] M-Y Chiu, U-S Jeng, C-H Su, K. S. Liang, K. H. Wei, Adv. Mater. 20 (2008) 2573

[4.16] R. J. Kline, M. D. McGehee, E. N. Kadnikova, J. Liu, J. M. J. Frechet, Adv. Mater. 15 (2003)1519.

[4.17] B. E. Warren, X-ray diffraction, Dover, New York (1990)

[4.18] D. Cullity, Elements of X-ray diffraction, Addison-Wesley, Reading, MA (1956)

[4.19] M. Drees, H. Hoppe, C. Winder, H. Neugerbauer, N. S. Sariciftci, W. Schwinger, F. Schaffler, C. Topf, M. C. Schraber, Z. Zhud, J. Mater. Chem. 15 (2005) 5158

[4.20] D. E. Motaung, G. F. Malgas, C. J. Arendse, S. Mavundla, C. J. Oliphant, D. Knoesen, J. Mater. Sci. 44 (2009) 3192

SUMMARY

One major drawback of organic photovoltaics (OPVs), besides its stability, is its low overall power conversion efficiency compared to the established inorganic solar cells, such as mono-crystalline silicon. There are several factors that influence the efficiency of OPVs, e.g. the structure of the polymer, the morphology of the film, the interfaces between the layers, the choice of electron acceptor material and the ratio between the electron acceptor material and the polymer.

In this project regioregular poly(3-hexylthiophene) (rr-P3HT) was used as the electron-donor material and [6,6]-phenyl-C_{61}-butyric acid methyl ester (PCBM) was employed as an electron-acceptor material. The aim of this study was to find the optimal blend ratio of rr-P3HT:PCBM for effective charge transfer and hence an improved efficiency. To achieve this, the optical properties of different blend ratios were probed and related to the structural changes that occurred within these materials.

In Chapter 3 the optical properties of rr-P3HT and rr-P3HT:PCBM blended thin films were studied using UV-VIS and PL spectroscopy. The absorption of rr-P3HT in the visible range showed a significant blue shift with an increase in PCBM loading in the blended thin film (1:4 ratio), which was attributed to the lowering of the interchain interaction and a non photo-induced charge transfer process between rr-P3HT and PCBM in the solid state. The interaction between the rr-P3HT and PCBM not only

reduced the order within the polymer chain, which is detrimental for charge transport, but also increased the mismatch between the absorption spectra of the blended thin films and the solar emission spectrum. The PL results showed improved quenching when the polymer is blended with PCBM in a 1:1 weight ratio, which indicated superior charge transfer from the polymer donor to the PCBM acceptors, due to a finer phase separation in this blend ratio. Further loading with PCBM to a 1:4 ratio resulted in a reduced quenching and was attributed to the ineffective charge transfer process caused by the formation of phase separated clusters or agglomerates of PCBM islands within the polymer matrix.

In Chapter 4 the structural properties of rr-P3HT films and rr-P3HT:PCBM blended films were investigated using FTIR spectroscopy, Raman spectroscopy, XRD and HR-TEM. The changes in the structural properties were correlated with changes in the optical properties.

Quantitative analysis of the FTIR absorption peak at 834 cm^{-1} confirmed the reduction in structural disorder in rr-P3HT, induced by blending it with excessive amounts of PCBM. These results were further corroborated with Raman spectroscopy, which for the 1:4 blend showed a shift to higher wavenumbers for the C=C stretching deformation peak centred around 1450 cm^{-1}, indicative of an increased disordering in the conjugated polymer.

XRD and HR-TEM demonstrated the crystalline behaviour of rr-P3HT and the 1:1 blend. However, the crystal sizes decreased with an increase in PCBM weight ratio, which suggested a more disordered film with smaller crystalline domains. This

supported the interpretation of the spectroscopic and optical measurements. Finally, the d-spacing obtained from XRD and HR-REM indicated a preferred orientation of rr-P3HT on the sample surface

In summary, light absorption by rr-P3HT:PCBM blends followed by charge transfer, delocalisation and transport of charge carriers within the bulk heterojunction is sensitive to the amount and size of PCBM clusters. An excessive PCBM concentration (1:4 weight ratio) leads to the formation of voluminous PCBM clusters. The PCBM surplus at higher PCBM concentrations is no longer homogeneously dispersed within the polymer matrix, but diffuses away and creates phase-separated clusters. An optimum weight ratio of rr-P3HT:PCBM = 1:1 results in a finer phase separation in this blend ratio. We therefore conclude that for an effective charge transfer mechanism and the subsequent improved efficiency in a heterojunction solar cell, a rr-P3HT:PCBM blend with weight ratio of 1:1 is recommended as the light absorbing active layer.

APPENDIX

HOOKE'S LAW

Molecular vibrations can be treated using Newtonian mechanics, to calculate the correct vibration frequencies. The basic assumption is that each vibration can be treated as though it corresponds to a spring. In the harmonic approximation the spring obeys Hooke's law: the force (F) required to extend the spring is proportional to the extension. The proportionality constant is known as a force constant, k.
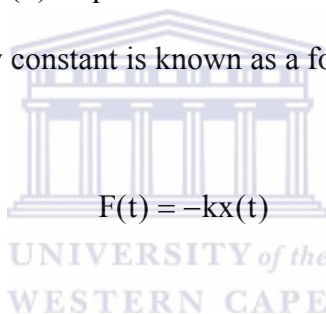
$$F(t) = -kx(t) \qquad (A1)$$

From Newton second law, the acceleration a(t) is now given as:

$$a(t) = \frac{F(t)}{m} = -\frac{kx(t)}{m} \qquad (A2)$$

The position of an object in a simple harmonic motion in one dimension is given by the following expression:

$$x(t) = A\sin(\omega t + \delta) \qquad (A3)$$

where ω is the angular frequency, δ is the phase and A is the amplitude.

Taking successive derivatives yields the velocity:

$$\upsilon(t) = \frac{dx(t)}{dt} = \omega A \cos(\omega t + \delta) \tag{A4}$$

and the acceleration;

$$a(t) = \frac{d}{dt}\upsilon(t) = -\omega^2 A \sin(\omega t + \delta) = -\omega^2 x(t) \tag{A5}$$

Therefore:
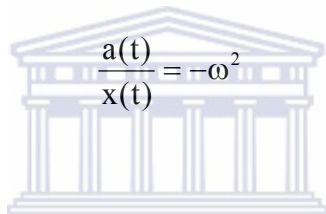
$$\frac{a(t)}{x(t)} = -\omega^2 \tag{A6}$$

Substituting (A6) into (A2) yields:

$$\omega = \sqrt{\frac{k}{m}} \tag{A7}$$

or, in terms of frequency ν:

$$\nu = \frac{1}{2\pi}\sqrt{\frac{k}{m}} \tag{A8}$$